Symmetric coupling of multiple timescale systems with Mixed-Mode Oscillations and synchronization

Soledad Fernández-García, Alexandre Vidal

Symmetric coupling of multiple timescale systems with Mixed-Mode Oscillations and synchronization

Soledad Fernández-García[1]

Dpto. EDAN&IMUS, University of Seville,
Campus de Reina Mercedes, 41012 Sevilla, Spain
EPI MYCENAE and ARAMIS, Inria Paris Research Center, France

Alexandre Vidal[2]

Laboratoire de Mathématiques et Modélisation d'Évry (LaMME), CNRS UMR 8071,
Université d'Évry-Val-d'Essonne, IBGBI, 23 Bld de France, 91037, Evry, France

Abstract

We analyze a six-dimensional slow-fast system consisting of two symmetrically coupled identical oscillators. Each oscillator is a three-dimensional slow-fast system formed by a FitzHugh-Nagumo model with an additional slow variable. Individually, each three-dimensional subsystem admits an attractive Mixed-Mode Oscillations limit cycle, featuring small oscillations due to the presence of a folded singularity. We consider a linear symmetric coupling of the fast variable of each oscillator upon one of the slow equations of the other one and study the synchronization properties between oscillators according to the value of the coupling gain parameter.

We examine theoretically and numerically both excitatory and inhibitory cases associated with positive and negative values of the coupling gain. Apart from *in-phase locking synchronization* and *antiphase synchronization* patterns, the coupled system generates *phase-locking almost-in-phase synchronization*, *relaxation loss of one of the oscillators* and *total oscillation death*, intertwined with complex transitions involving period doubling cascades, period adding phenomena and chaos. We present a theoretical proof of the behavior repartition ac-

[1]Corresponding author: soledad@us.es
[2]alexandre.vidal@univ-evry.fr

cording to the coupling gain parameter both in inhibitory and excitatory cases. In the case of antiphase synchronization, we prove the increase in the oscillation frequency of the 6D system asymptotic orbit as the negative coupling parameter value increases. In the case of excitatory coupling, we point out the role of Mixed-Mode Oscillations in the birth of almost-in-phase and in-phase locking synchronization patterns and the transitions between them.

Keywords: Slow-Fast Dynamics, Coupled Oscillators, Mixed-Mode Oscillations, Synchronization, Nonlinear Neuron Model.
2010 MSC: Primary: 34C15, 34C23, 34D06, Secondary: 70K70, 92B25.

1. Introduction

Neural synchronization is a basic functioning principle of the nervous system resulting from the coupling between the activities of different neurons (microscopic scale), neuronal ensembles (mesoscopic scale), and brain areas (macroscopic scale). At the microscopic scale, recent advances in optical imaging, have provided evidence that calcium activities measured *in-vivo* (e.g. in the zebrafish embryo [1]), exhibit characteristic synchronized behaviors in the brain, as well as in the spinal cord. The data[3] reveal a very strong synchronization (along the whole 4 minutes recording) of the oscillations in intracellular calcium levels between motoneurons located on the left and right side of the spinal cord respectively, while the activity profiles of these two clusters feature "antiphasic" properties: no calcium peak occur simultaneously in both clusters. A natural interpretation of these data points out the existence of an excitatory intra-cluster coupling and an inhibitory inter-cluster coupling.

To study theoretically the different features of synchronization in oscillatory patterns of intracellular calcium concentrations (ICC) between neurons,

[3]Fig. 1 in [1] : `https://arxiv.org/ftp/arxiv/papers/1407/1407.4380.pdf#page=19`

we propose a compact system composed by two coupled three-dimensional (3D) slow-fast systems, based on classical FitzHugh-Nagumo dynamics [2, 3]. This model has been originally designed for reproducing the changes in ICC of a single gonadotropin-releasing hormone (GnRH) expressing neuron [4], taking particular advantage of the Mixed-Mode Oscillations feature for reaching the quiescence/active phase duration ratio. While considering two coupled oscillators for representing the activity of clusters of strongly synchronized neurons is an oversimplification of the real network phenomenon, its simplicity allows us to perform singular perturbation analysis and study, at an aggregated level, the fundamental properties of the system in a formal way, and therefore to analyze the underlying dynamical mechanisms of synchronization between neurons and clusters in case of inhibitory or excitatory coupling.

Synchronization properties of systems with multiple timescales, as relaxation oscillators, are known to be different from harmonic ones [5, 6, 7, 8, 9, 10, 11, 12]. In particular, through the Fast Threshold Modulation coupling [13, 14, 15, 16], the synchronization is very rapid and relatively independent from the coupling strength. The impact of canard phenomena in weakly coupled slow-fast systems has been studied in several works that analyze different questions, such as synchronization and/or desynchronization [17, 18, 19, 20, 21], localized oscillatory patterns and formation of clusters [18, 22, 21]. Mechanisms underlying synchronization of systems presenting bursting activity (alternation of slow quiescent phases and fast oscillatory phases) are analyzed in [23, 24, 25, 26].

The usual coupling between computational neuron models considered in the literature is either electrical (gap junction) or synaptic, since they are generally designed for studying the neuron-neuron communication. In both cases, the coupling between slow-fast neuron models impact the fast variable. In our study, we focus on the underlying dynamics of ICC, on which the transmission through synapses or gap-junctions between neurons has a marginal effect. For instance, it has been shown in [27] that spontaneous postsynaptic currents of cultured motoneurons from the rat did not elicit significant ICC transients. Significant elevations of ICC result from release of calcium from the endoplasmic

reticulum through calcium-induced calcium release (CICR) mechanism. The dominant channel of CICR involves the non neuronal glial cells, especially the astrocytes, and the elevation of Inositol trisphosphate (IP3) from neighbor to neighbor through gap junction (see for instance [28, 29, 30]). This regulation mechanism is slower than neuronal transmission [31], yet it is central in the functional neuron-glia system and dysfunctions of the signaling pathway have been identified as playing a major role in motoneuron diseases [32, 33].

Following a phenomenological approach, which consists in selecting the dynamics according to the consistency between the model outputs and experimental observations, we have chosen the coupling via the slow recovery variable, which represents the appropriate timescale of the above mechanism. In this type of coupling, the critical manifold of each oscillator (set of singular points of the fast dynamics) is invariant by the coupling parameter. Consequently, the coupling strength does not impact the critical manifold of the whole slow-fast coupled system either.

Such kind of coupling has already been considered. In [34, 35, 36, 37], the coupling is one-way between two planar FitzHugh-Nagumo systems to mimick the slow regulation of the GnRH secretory system by the interneuron network that conveys the steroid feedback. In [38], a rigorous study of signature transitions in Mixed-Mode Oscillations (MMOs) generated by such system has been performed. More recently, in [20], a bidirectional coupling of this type between two planar systems was considered. In [19, 39], a system is built using such type of coupling between three planar oscillators, two connected bidirectionally and a third one that acts as a regulator, connected one-way to the other two. In this work, we consider another extension of coupled slow-fast systems using a bidirectional coupling between two 3D systems.

The new variable added to the classical FitzHugh-Nagumo system enables the emergence of MMOs in the orbits of the 3D oscillators, which makes the dynamics of the coupled six-dimensional (6D) system richer than the coupling of relaxation oscillators and harder to analyze. In this article, we propose an insight on the synchronization of coupled Mixed-Mode Oscillators, that is known

to be a very difficult and yet fascinating question, from a perspective that we want to be global in two senses. First, we consider the global asymptotic behavior of the 6D system orbits and not only the local dynamics in the vicinity of the folded singularity. Second, we study the synchronization features for any coupling parameter values (both positive and negative). For medium positive values of the coupling parameter, instead of a quick *in-phase synchronization* pattern, we observe *phase-locking almost-in-phase synchronization* pattern, depending strongly on the strength of the coupling parameter. For the sake of brevity, we refer to this pattern as *almost-in-phase synchronization* from now on. Furthermore, for negative values, apart from *antiphase synchronization* patterns, the system also presents nonsymmetric behaviors: the *relaxation loss* of one oscillator and the *total oscillation death.* In this study, we describe and prove the distribution of these asymptotic behaviors according to the value of the coupling gain parameter. We also illustrate numerically and discuss the dynamical mechanisms involved in the transitions between behaviors.

The article is outlined as follows. In Section 2, we first recall the properties of the 3D slow-fast oscillator introduced in [4], we then introduce the symmetric coupling between two such oscillators considered in this work and describe the main asymptotic patterns generated by the system. In Section 3, we describe the main asymptotic behaviors of the 6D system and prove their repartition according to the value of the coupling gain parameter. We then prove that when the coupling parameter c is negative, the oscillation frequency increases as c increases, that is, as $|c|$ decreases. In Section 4, we show the complexity of the changes in the (quasi)-periodic behaviors for weak coupling. Basing ourselves on numerical simulations, we discuss the role of MMOs in organizing the dynamics for such coupling. Finally, in Section 5, we discuss possible extensions of the present work. The entire technical proofs of each result are available in Appendices.

2. Model properties

This section is divided into five subsections. We first recall the main properties of the 3D slow-fast oscillator introduced in [4]. Then, we focus on canard-induced MMOs of the system. In the third subsection, we introduce the symmetric coupling between two identical 3D oscillators. We introduce the main asymptotic patterns generated by the 6D system. Using simulations, we introduce in the last subsection the repartition of the main behaviors that will be theoretically analyzed in the sequel.

2.1. Three-dimensional slow-fast oscillator

The 3D slow-fast system introduced in [4] for modeling the dynamics of the ICC in a single neuron reads

$$\dot{x} = \tau(-y + f(x) - \phi_f(z)), \tag{1a}$$

$$\dot{y} = \tau\varepsilon(x + a_1 y + a_2), \tag{1b}$$

$$\dot{z} = \tau\varepsilon\left(\phi_r(x) - \frac{z - z_b}{\tau_z}\right), \tag{1c}$$

where

$$\phi_f(z) = \frac{\mu z}{z + z_0}, \tag{2}$$

$$\phi_r(x) = \frac{\lambda}{1 + \exp(-\rho(x - x_{on}))}, \tag{3}$$

where $(x, y, z) \in \mathbb{R}^3$ and the overdot denotes the derivative with respect to time variable t. The timescale separation parameter fulfills $0 < \varepsilon \ll 1$. Function f is an odd cubic function such that $y = f(x)$ is an S-shaped curve: f admits a local minimum at $x = -x_f < 0$ and a local maximum at $x = x_f > 0$. Without loss of generality, we can (and, in the following, we will often) consider $f(x) = -x^3 + 3x_f^2 x$. Parameter $\tau > 0$ has been introduced in [4] for the outputs to meet a given physical timescale and does not impact the phase portrait. Moreover, we assume $a_1 < 0$, $|a_1| \ll 1$ (in a sense specified in the following) and parameters $a_2, z_0, \lambda, \tau_z, z_b$ to be strictly positive. We also consider a large

enough ρ value such that the sigmoid ϕ_r is steep at its inflection point and, therefore, represents a sharp activation function.

Subsystem (1a)-(1b) is built on a classical FitzHugh-Nagumo system [2, 3], where the fast variable x represents the electrical activity of the cell and the slow variable y is a recovery variable. Originally, the additional slow variable z represents the ICC in a single neuron. The dynamics of variable z is mainly driven by the increasing sigmoidal function ϕ_r, and it acts as a feedback onto the x dynamics through the Hill function ϕ_f bounded by μ. When $\phi_r(x)$ is inactive (close to 0), variable z decreases to a quasi steady state close to z_b which represents the baseline of the intracellular calcium level. The exponential decay rate of this motion is given by $\tau\varepsilon/\tau_z$. The effect of this coupling is to reduce the electrical activity of the neuronal population in response to the rise of intracellular calcium concentration. An analogous term is used in models of single neurons to represent the hyperpolarization of the cell membrane stimulated by calcium [40]. More generally, in this article, we consider system (1) fulfilling the above assumptions as a typical class of slow-fast system with 1 fast and 2 slow variables able to generate canard-induced MMOs as explained in the following.

In order to describe the behavior of the system, we specify the nullclines and possible stationary states.

- The $x-$nullcline is the critical manifold

$$S \equiv \{y = f(x) - \phi_f(z)\}\,. \tag{4}$$

It is an S-shaped surface with two fold lines:

$$\mathcal{F}^- \equiv \{x = -x_f,\, y = f(-x_f) - \phi_f(z)\}\,, \tag{5}$$

and

$$\mathcal{F}^+ \equiv \{x = x_f,\, y = f(x_f) - \phi_f(z)\}\,. \tag{6}$$

The fold lines split the critical manifold into three sheets. The left and right sheets (contained in $x < -x_f$ and $x > x_f$, respectively) are attracting for the fast dynamics, and we will note them S_l and S_r, respectively. The

middle sheet S_m (contained in $|x| < x_f$) is repulsive. From geometric singular perturbation theory [41], the part of these sheets away from the folds perturbs, for small enough positive values of ε, into slow manifolds $S_{l,\varepsilon}$, $S_{r,\varepsilon}$ and $S_{m,\varepsilon}$, invariant for system (1), and lying in a $O(\varepsilon)$-neighborhood of S_l, S_r and S_m, respectively. Note that the $O(\varepsilon)$ proximity between the sheets of the critical manifolds and the respective slow manifolds relies on the Hausdorff distance applied to the compact submanifolds of these sheets. The left and right slow manifolds are exponentially attractive w.r.t. ε while the middle one is exponentially repulsive. Moreover, considering the extensions of $S_{l,\varepsilon}$ (resp. $S_{r,\varepsilon}$) by the positive flow, its first intersection with $x = -x_f$ (resp. $x = x_f$) is a curve $O(\varepsilon^{2/3})$-close to the lower fold $\mathcal{F}_-$ (resp., the upper fold $\mathcal{F}_-$). For more details on these results (that are now considered as classical), we refer the reader to [38, 42, 43, 44, 45, 46], for instance.

- The $y-$nullcline is the plane

$$\Pi \equiv \left\{ y = -\frac{x + a_2}{a_1} \right\}. \tag{7}$$

- The $z-$nullcline is the sigmoidal surface

$$\Gamma \equiv \left\{ \phi_r(x) - \frac{z - z_b}{\tau_z} = 0 \right\}. \tag{8}$$

  In order to give the approximate location of the system equilibria, we consider the Heaviside approximation of the sigmoidal function ϕ_r obtained for $\rho \to \infty$. This leads to the approximation:

$$\Gamma \simeq \begin{cases} \{z = z_b\}, \text{ if } x < x_{on}, \\ \{z = z_b + \lambda\tau_z =: z_h\}, \text{ if } x > x_{on}. \end{cases}$$

As in the original FitzHugh-Nagumo system, we take $|a_1|$ small enough to ensure that the x and y nullclines intersect only once for any fixed z value. Thus, we define the following special curves lying on the critical manifold

$$S_b \equiv \{y = f(x) - \phi_f(z_b), \quad x < x_{on}, \quad z = z_b\}, \tag{9}$$

$$S_h \equiv \{y = f(x) - \phi_f(z_h), \quad x > x_{on}, \quad z = z_h\}. \tag{10}$$

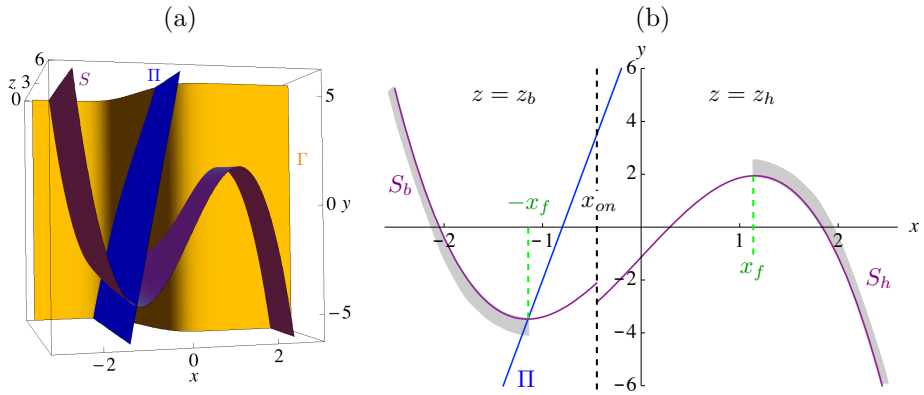

Figure 1: Nullclines of system (1). Panel (a): x, y and z-nullclines are the purple, blue and yellow surfaces, respectively. Panel (b): Representations in the same (x, y)-plane of the half-planes $z = z_b$ for $x < x_{on}$ and $z = z_h$ for $x > x_{on}$. Thus, the purple lines are the approximations S_b and S_h given in eqs. (9) and (10). The blue straight line represents the projection of the y-nullcline Π. The grey area close to S_b (resp. S_r) is the projection of the attractive sheet S_l (resp. S_r) of the fast dynamics for $z \in [z_b, z_h]$.

In the following, when necessary, we will mention the use of an approximation of the equilibrium point by the intersection between S_b or S_h and plane Π. In particular, such approximations allow us to greatly simplify the illustrations of the nullclines positions in a 2D view (see Fig. 1). Moreover, note that the projection of $S_l \cap \{z_b \leq z \leq z_h\}$ is well-approximated by the part of S_b on the left of the lower fold, and the projection of S_r is well-approximated by the part of $S_h \cap \{z_b \leq z \leq z_h\}$ on the right of the upper fold.

For the simulations shown in this article, we have used $f(x) = -x^3 + 4x$, and the following parameter values:

$$\begin{array}{lllll} a_1 = -0.1, & a_2 = 0.8, & \varepsilon = 0.06, & \tau = 37, & z_0 = 5, \\ z_b = 1, & \tau_z = 2, & x_{on} = -0.45, & \lambda = 1.75, & \rho = 30. \end{array} \tag{11}$$

2.2. Mixed-Mode Oscillations of the 3D system

In Appendix A, we prove that for $\mu = 2.51$, system (1) admits a folded saddle-node type II (FSNII) singularity in the singular limit, which implies that a singular Hopf bifurcation occurs within a $O(\varepsilon)$-distance in the parameter space

and that for $\mu < 2.51$, system (1) admits a folded node (FN) singularity. It is well-known that in the unfolding of the FN and the FSNII singularities, systems generate canard-induced MMOs [42, 43, 45, 47, 48, 46]. In particular, in [46], the author have proven the existence of a "funnel", i.e. a partition of the local phase space by "sectors of rotation", that organizes the local dynamics near FN type singularities. The sectors are separated by secondary canards corresponding to intersections between the attractive left and repulsive middle slow manifolds ($S_{l,\varepsilon}$ and $S_{m,\varepsilon}$, respectively). Then, the number of small oscillations featured by a local orbit depends on the specific sector of rotation of the associated funnel that it enters. Together with the global return mechanism provided by the cubic term in the $x-$nullcline, the existence of such folded singularity allows system (1) to generate MMOs. We refer the reader to the seminal article [46] and to the review [49] and references therein for more details about canard-induced MMOs. We recall the three qualitatively different behaviors depending on the position of the equilibrium point, since we will refer to their features in the subsequent analysis of the coupled system. We recall that the following description results from a slow-fast analysis and thus we consider $\varepsilon > 0$ small enough, which means, rigorously, that there exists a fixed value $\varepsilon_0 > 0$ such that the statements are fulfilled for any $\varepsilon \in]0, \varepsilon_0]$ (see [41]).

The three cases described below refer to the panels displayed in Fig. 2.

(a) The equilibrium lies on the middle sheet of the critical manifold S and far from the folds: the equilibrium is unstable and the system admits a globally attractive limit cycle of relaxation type.

(b) The equilibrium lies on the middle sheet S_m of S and close to a fold: the equilibrium is unstable and the system generates MMOs.

(c) The equilibrium lies on S_l: the equilibrium is stable and the system asymptotically reaches a steady state. A similar situation occurs if the equilibrium lies on S_r (not shown in the figure).

It is worth describing the path of x along a prototypical MMO limit cycle (case (b)) of system (1), in order to better understand the behavior of the

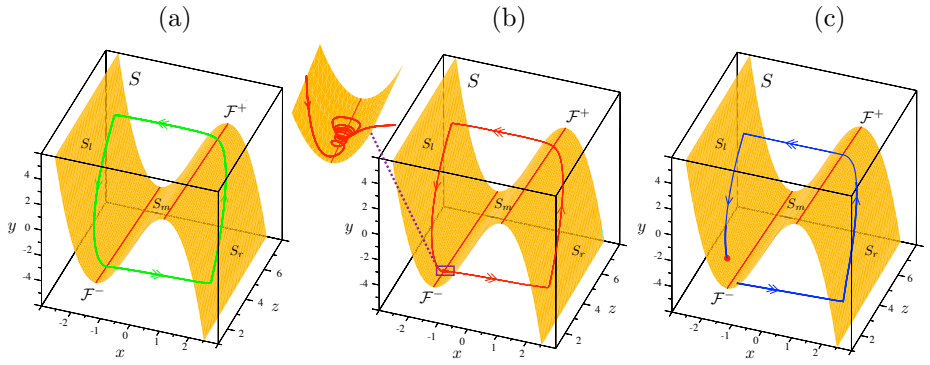

Figure 2: Main behaviors of the single oscillator. Panel (a): relaxation oscillation. Panel (b): Mixed-Mode Oscillation (with a magnified view on the small oscillations). Panel (c): no sustained oscillation; the red point is an attractive equilibrium.

coupled system later. We note $\hat{\mathbf{p}} = (\hat{x}, \hat{y}, \hat{z})$ with $\hat{x}$ close to $-x_f$ the unique equilibrium point of system (1), which is unstable; we denote by $x_{\min}$ (resp. $x_{\max}$) the minimal (resp. maximal) value of x along the limit cycle and $P = (x, y, z)$ the current point. Recall that the folds $\mathcal{F}^-$ and $\mathcal{F}^+$ of the critical manifold S given by eq. (4) are located at $x = -x_f$ and $x = x_f$ (see eqs. (5)-(6)). Also, we consider the special curves S_b and S_h given by eqs. (9)-(10) as the approximation of the intersections between the z-nullcline and the right and left sheets of the critical manifold, respectively.

Consider the projection $\mathcal{F}^-_{proj}$ of $\mathcal{F}^-$ along the x-direction (fast fibers) onto the opposite branch S_r of the critical manifold (see Fig. 3). The x-component of the intersection between $\mathcal{F}^-_{proj}$ and the special curve S_h is the unique positive solution of $f(x) - \phi_f(z_h) = f(-x_f) - \phi_f(z_b)$, that we denote x_M. Analogously, consider the projection $\mathcal{F}^+_{proj}$ of $\mathcal{F}^+$, along the x-direction (fast fibers) onto the opposite branch S_l of the critical manifold. The x-component of the intersection between $\mathcal{F}^+_{proj}$ and the special curve S_b is the unique negative solution of $f(x) - \phi_f(z_b) = f(x_f) - \phi_f(z_h)$, that we denote x_m.

Now along the limit cycle, starting close to $S_{r,\varepsilon}$, which is attractive, and with $z_b < z < z_h$, $\dot{y} > 0$ and $\dot{z} > 0$, it holds that: the current point P climbs up along $S_{r,\varepsilon}$ until it reaches $\mathcal{F}^+$ vicinity and z remains below z_h. From classical

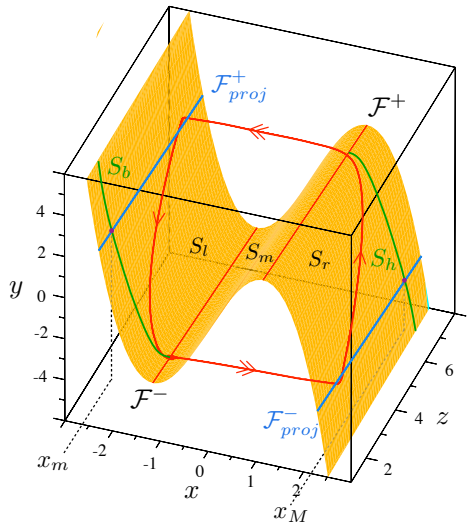

Figure 3: Construction of x_M (resp. x_m) as the x-component of the intersection point between $\mathcal{F}^-_{proj}$ and the special curve $S_h = \{y = f(x) - \phi_f(z_b), x < x_{on}, z = z_b\}$ (resp. $\mathcal{F}^+_{proj}$ and the special curve $S_b = \{y = f(x) - \phi_f(z_h), x > x_{on}, z = z_h\}$.

results on fold-induced slow-fast transitions [44], $S_{r,\varepsilon}$ crosses at $O(\varepsilon^{2/3})$ vicinity of $\mathcal{F}^+$ and, under the impact of the fast dynamics, reaches S_l $O(\varepsilon^{2/3})$-close to $\mathcal{F}^+_{proj}$. Once P crosses the critical manifold, $\dot{x} > 0$ and consequently $x_{\min} \approx x_m$. Then, $\dot{y} < 0$ and $\dot{z} < 0$: P follows $S_{l,\varepsilon}$ towards the lower fold. The equilibrium point $\hat{\mathbf{p}}$ is both unstable and ε-close to the lower fold. Yet, recall that we consider the limit cycle to enter the funnel of the folded singularity away from any secondary canard. Hence, despite the fact that small oscillations occur near $\mathcal{F}^-$, a similar fast motion occurs from the fold vicinity towards the opposite branch: P reaches S_r ε-close to $\mathcal{F}^-_{proj}$ and, since $\dot{x} < 0$ once P has crossed S_r, we obtain $x_{\max} \approx x_M$.

Hence, one period of an MMO limit cycle can be divided into five phases. In the following description, we focus on the path of variable x:

I. Silent phase: P follows $S_{l,\varepsilon}$ exponentially close (w.r.t. ε) while x increases from $x_{\min}$ to $-x_f - \delta_\varepsilon$ with δ_ε is of order $O(\varepsilon)$ and positive.

II. Passage through the funnel: P undergoes small oscillations during the

passage through the funnel near the fold $\mathcal{F}^-$ and $x \in (-x_f - \delta_\varepsilon, -x_f + \delta_\varepsilon)$.

III. Jump-up: P follows an almost horizontal (y and z almost constant) fast fiber to reach $S_{r,\varepsilon}$ vicinity and $x \in (-x_f + \delta_\varepsilon, x_{\max})$,

IV. Active phase: P climbs up exponentially close (w.r.t. ε) to $S_{r,\varepsilon}$ up to the upper fold $\mathcal{F}^+$ while x decreases from $x_{\max}$ to x_f.

V. Jump-down: P follows a fast fiber to reach $S_{l,\varepsilon}$ vicinity and x decreases from x_f to $x_{\min}$.

We will refer to Phases I to V of a MMO limit cycle in the whole article.

Recall that, even if all orbits (except orbits reduced to a singular point of the system) eventually adopt the above behavior, chaotic dynamics may arise for certain range of parameter values. Such a situation is characterized as follows (see [47, 45, 49] for instance). Consider the global return map π (Poincaré map), defined from a section Σ transverse to S_l away from the folded singularity into itself: the image of $P \in \Sigma$ by this map is defined as the first intersection point between Σ and the positive trajectory starting from P. Note that the trajectory between P and $\pi(P)$ necessarily features a relaxation oscillation or at least a sufficiently large excursion in the phase space. If π admits a single fixed point, it is associated with an attractive limit cycle, featuring a single relaxation and n small oscillations along one period (signature 1^n): such cycle stays sufficiently far away from the secondary canards and spirals around the pseudo-singularity following one sector of rotation associated with n small oscillations. When the unicity of the fixed point is lost by varying a parameter value, several periodic orbits appear. In particular, the existence of multiple fixed points for π close to the intersection with a secondary canard reveals the non existence of limit cycle and the existence of quasi-periodic orbits or non isolated periodic orbits with complex signature $1^{s_1}1^{s_2}...1^{s_p}$, where $s_i \in \{n, n+1\}$). In such case, along any orbit, the current point passes recurrently close to a secondary canard, on one side or the other at each passage, and therefore generates n or $n+1$ small oscillations.

For the sake of simplicity, in the following, we consider ranges of parameter

values such that the 3D oscillator (1) admits an attractive MMO limit cycle featuring small oscillations near the lower fold $\mathcal{F}^-$, which we state as hypothesis in the whole article. We consider two identical 3D systems of type (1), and aim at understanding how they interact when they are symmetrically coupled.

2.3. Symmetric coupling of two identical systems

We consider a symmetric linear coupling through the fast variable in the slow dynamics of the recovery variable between two identical oscillators:

$$\begin{array}{ll} O_1 & \left\{ \begin{array}{l} \dot{x} = \tau(-y + f(x) - \phi_f(z)), \\ \dot{y} = \tau\varepsilon(x + a_1 y + a_2 + c(x - X)), \\ \dot{z} = \tau\varepsilon \left(\phi_r(x) - \dfrac{z - z_b}{\tau_z} \right), \end{array} \right. \\ O_2 & \left\{ \begin{array}{l} \dot{X} = \tau(-Y + f(X) - \phi_f(Z)), \\ \dot{Y} = \tau\varepsilon(X + a_1 Y + a_2 + c(X - x)), \\ \dot{Z} = \tau\varepsilon \left(\phi_r(X) - \dfrac{Z - z_b}{\tau_z} \right), \end{array} \right. \end{array} \tag{12}$$

with c either positive or negative. For the sake of simplicity, in the following, we will refer as O_1 and O_2 to each oscillator undergoing the impact of the fast variable of the other one. Hence O_1 is the X-dependent subsystem of variables (x, y, z) and O_2 is the x-dependent subsystem of variables (X, Y, Z). Remark that the coupling is not involved in the fast dynamics and, consequently, the critical manifolds of O_1 and O_2 are defined by the same equations in (x, y, z) and (X, Y, Z) spaces, respectively. Hence, we keep in mind that these manifolds do not belong to the same space, but that they are the exact same geometric object S as parameterized in eq. (4). In the following, for simplifying the notations as long as the context does not lead to ambiguous interpretation, we will equally refer to the critical manifold of O_1 and O_2 as S and to the left and right sheets as S_l and S_r.

First, remark that if we consider the same initial conditions for both oscillators $(x_0, y_0, z_0) = (X_0, Y_0, Z_0)$, the coupling terms do not affect the dynamics: $x = X$ for any time and consequently $y = Y$ and $z = Z$ for any time as well. Along such orbit, both oscillators O_1 and O_2 behave exactly in the same way.

Moreover, both admit the same unstable equilibrium point close to the lower fold of their critical manifold and the same MMO limit cycle. Consequently, the two oscillators are in-phase synchronized and generate MMOs. The 3D subspace $\{x = X, y = Y, z = Z\}$ is therefore an invariant space where there always exist an equilibrium point of the 6D system (12) and a MMO limit cycle that is attractive inside this subspace.

If we consider different initial conditions, the coupling terms play different roles depending on the sign and strength of parameter c, resulting in different dynamical behaviors that we analyze in the sequel. Hence, for the sake of simplicity, we will only refer to the asymptotic behavior (ω-limit) of the orbits of system (12) with any initial data that is not a singular point and outside $\{x = X, y = Y, z = Z\}$, keeping in mind that, in this invariant subspace, the sole asymptotic behavior is obtained as the same MMO limit cycle for both oscillators with no phase-shift between them.

2.4. Main asymptotic behaviors of the coupled system

We describe the main asymptotic behaviors, i.e., those occurring for large intervals of c values. In Panel (0) of Fig. 4, we represent the time traces of (x, X) and (z, Z) variables along an orbit of system (12) of two identical uncoupled ($c = 0$) oscillators in MMO regime with different initial conditions.

If $c \neq 0$, system (12) with different initial conditions for O_1 and O_2 can generate different patterns depending on the value of the coupling parameter c. Note that we have produced the simulations presented in this section with $\mu = 2.4$, but one can consider equally neighboring value of μ close to 2.51 (value obtained in the Appendix A) for which system (12) admits an attractive MMO limit cycle, and obtain the same dynamical cases yet for different ranges of the coupling parameter c. We represent an instance of each case in Fig. 4 and we explain each asymptotic behavior below.

(a) *Total oscillation death:* both oscillators reach a stable equilibrium.

(b) *Relaxation loss:* one of the oscillators produces relaxation oscillations between S_l and S_r, while the other oscillates confined near S_l.

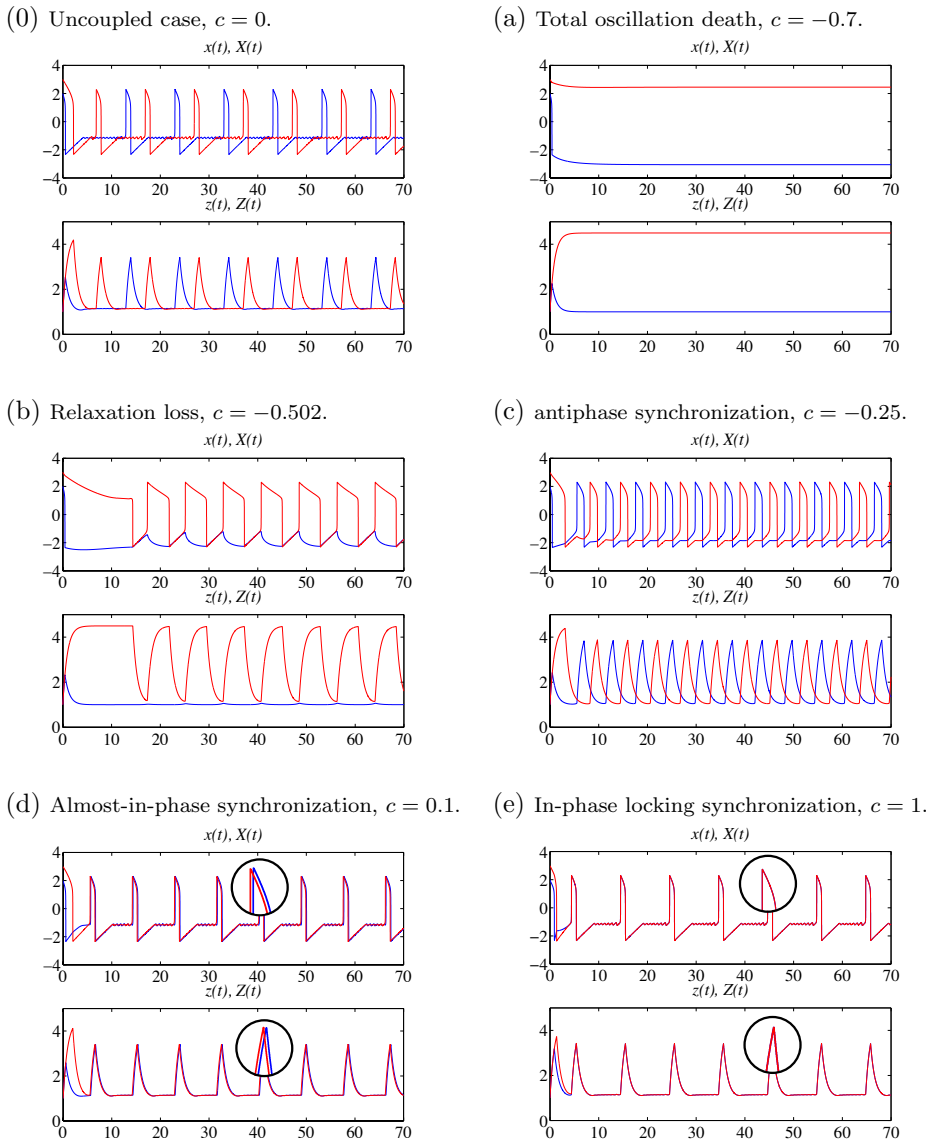

Figure 4: Patterns generated by system (12) according to the values of c. The other parameter values are given by 11 and $\mu = 2.4$. We emphasize the difference between almost-in-phase and in-phase locking synchronization cases with magnified views on the shifted signals generated by O_1 and O_2 in panel (d) and on coincident signals in panel (e), despite the different initial conditions taken for the two oscillators.

(c) *Antiphase synchronization:* the oscillators follow the exact same orbit, with a half-period phase-shift.

(d) *Almost-in-phase synchronization:* the oscillators follow the exact same orbit, yet there exists a phase-shift between them.

(e) *In-phase locking synchronization*: the oscillators follow the exact same orbit, which coincides with the attractive limit cycle of the uncoupled case. In this case, the limit cycle lying on $\{x = X, y = Y, z = Z\}$ is a global attractor of the system.

Note that behavior (a) should be interpreted as out of the model limits since one expects imminent death of a neural cell featuring such a long uninterrupted activation. Yet it shows that the model reproduces the saturation of intracellular calcium concentration even in such extreme condition.

2.5. Overview of the macroscopic structure of the bifurcation diagram with respect to c.

We first present a synoptic view of the repartition of the behaviors characterized by the synchronization features presented in subsection 2.4 according to parameter c value. With this aim, we introduce sequences of return times and phase shifts between the two oscillators O_1 and O_2, as follows. We denote $(x_c(t), y_c(t), z_c(t), X_c(t), Y_c(t), Z_c(t))$ the solution of the coupled system for a fixed value of c starting from an initial condition that does not belong to the subspace $\{x = X, y = Y, z = Z\}$. We have simulated the solutions for each value of c on a 10^{-3} step grid of $[-1, 1]$ as long as necessary:

- either for the current point to enter the 10^{-3}-radius ball defined by the euclidian distance centered at the stable equilibrium point (case of total oscillation death, panel (a) in Fig. 4),
- or for the orbit to cross $\{x = 0, y < 0\}$ or $\{X = 0, Y < 0\}$ a hundred times (oscillatory cases, panel (b) to (e) in Fig. 4).

For each value of c in the grid corresponding to the second case above, we have kept the 26 last crossing times, denoted $(t_i^{x=0}(c))_{i=0}^{25}$ and $(t_i^{X=0}(c))_{i=0}^{25}$ in the

following. When applicable, we have calculated the successive return times:

$$T_i^{x=0}(c) = t_i^{x=0}(c) - t_{i-1}^{x=0}(c), \tag{13}$$

$$T_i^{X=0}(c) = t_i^{X=0}(c) - t_{i-1}^{X=0}(c), \tag{14}$$

with $i \in [1, 25] \cap \mathbb{N}$, and the non-oriented phase shifts between the two oscillators

$$\phi_i(c) = |t_i^{x=0}(c) - t_i^{X=0}(c)|. \tag{15}$$

Illustrative construction of crossing values, return times and shifts on an instance of $x(t)$ and $X(t)$ signals along an orbit of system (12) is shown in Fig. 5.

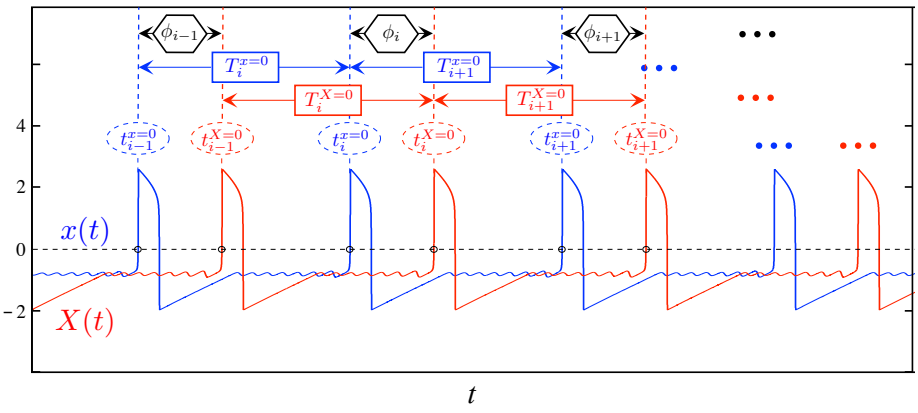

Figure 5: Illustration of the definitions of O_1 and O_2 crossing times and return times sequences and sequence of shifts between them on an instance of system (12) orbit.

From the features of the sequences of return times and shifts obtained for a fixed value of c, we can identify the asymptotic behavior reached by the simulated orbit. Indeed, the above construction can directly show if both oscillators reach a stable equilibrium vicinity, which leads to *total oscillation death*. A finite number of crossing time values $t_i^{x=0}(c)$ (resp. $t_i^{X=0}(c)$) while the sequence of the other one is non finite, indicates the *loss of relaxation* of O_1 or O_2. The convergence of the return times $T_i^{x=0}(c)$ and $T_i^{X=0}(c)$ sequences indicates that the orbit converges towards an attractive limit cycle such that, along one period, O_1 and O_2 undergo one and only one active phase (phase during which

x, resp. X, remains positive). The existence of multiple isolated adherence values of the sequences indicates the convergence towards a more complicated limit cycle such that, along one period that happens to be longer than in the preceding case, multiple activation phases of O_1 and O_2 occur. Scattered values of the return times indicate a quasi-periodic behavior and the chaotic feature of the dynamics. For fixed values of c, the sequence of shifts values between O_1 and O_2 naturally features the same convergence properties as the return times sequences: existence of a limit or multiple isolated adherence values or scattered values. Yet, additionally, the convergence of the shifts sequence towards 0 shows asymptotic *in-phase locking synchronization* between O_1 and O_2 while the convergence towards a single non zero value shows asymptotic *almost-in-phase synchronization*. A particular situation of this second case arises when the limit of the shift coincides with half the limit of the return times, which indicates *perfect antiphase synchronization* between O_1 and O_2.

Figure 6 shows, for each c value in the 10^{-3} step grid of $[-1, 1]$, the return times $(T_i^{x=0}(c))_{i=1}^{25}$ (blue points) and $(T_i^{X=0}(c))_{i=1}^{25}$ (green points), respectively and the phase shifts $(\phi_i(c))_{i=1}^{25}$ (red points). An animated view of the signals generated by x and X for various c values together with the picture of Fig. 6 is provided as supplemental material (see animated Fig. 7).

From this simulation, we identify five different intervals of c values labeled from A to E and corresponding to different general behaviors. Before specifying these behaviors, we emphasize an important point: while intervals D and E are separated by a single value c^p, it is not the case between A and B, B and C, C and D. Precisely, complex changes in the phase portrait occur for c values in small intervals around the specific value c^d, c^0 and 0, materialized in Figure 6. In this subsection, we mainly focus on the asymptotic behaviors displayed by the system outside small neighborhoods of these values. The changes occurring around c^d and c^0 are partly explained in the analysis presented in subsection 3.2 and approximations of these values are derived. The chaotic transitions occurring for c around 0 and in interval D are the subject of Section 4, where we provide magnified views of the simulations performed on a fine grid of c

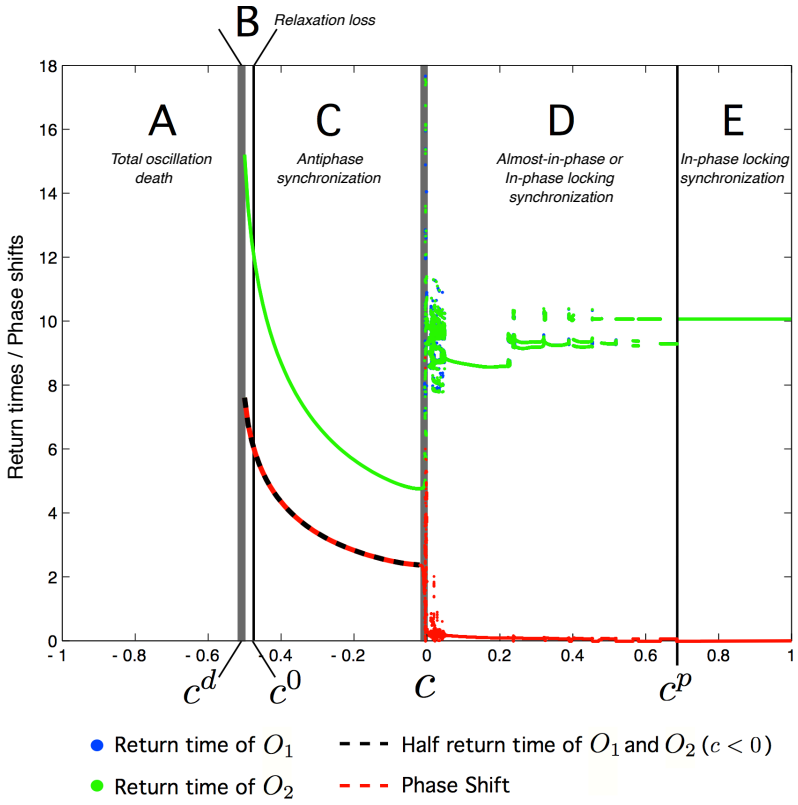

Figure 6: Synoptic view of the different synchronization patterns described in Theorem 3.1, depending on the value of the coupling parameter $c \in [-1, 1]$. The other parameter values are given by 11. For each value of c in intervals B to E, 25 return times for each oscillator (blue and green points) and 25 phase shifts are plotted. Blue points are hidden behind green points since they almost coincide for c value in intervals C and E and most of values in interval D.

values.

For c in interval A, both oscillators reach a stable equilibrium (panel (a) of Figure 4) and, consequently, no return times can be plotted. In interval B of c values, the sequence of return times are only defined for the sole oscillator (O_2) undergoing relaxation, since the crossing times $t_i^{x=0}(c)$ of O_1 are not defined in that case corresponding to panel (b) of Fig. 4. Yet, for each c value in B, the 25 points materializing the successive return times of O_2 cannot be distinguished, showing the convergence of the return time sequence (convergence towards a

(Loading Video...)

Figure 7: Repartition of synchronization types between O_1 and O_2 for c from -1 to 1 with a $2\,10^{-3}$ step value. Top panel : 50 seconds signals generated by x and X after a transient of 250 seconds starting from an initial data outside $\{x = X, y = Y, z = Z\}$. Bottom panel : partition into 5 intervals A to E of c values according to the type of synchronization between oscillators, sequences of 25 O_1 and O_2 return times (blue and green points), shifts (red points), half return times in case of antiphase synchronization (dashed black line). The moving vertical red bar materializes the c value corresponding to the associated frame in the top panel.

limit cycle). Since interval B is very narrow, in order to emphasize the case of *relaxation loss of one oscillator*, we give as supplemental material an animated view of the signals generated by x and X for c values around this interval (see animated Fig. 8).

(Loading Video...)

Figure 8: Transition from *total death oscillation* to *antiphase synchronization* through *relaxation loss of one oscillator* for values of c varying from -0.53 to -0.48 with 10^{-3} step value. The animation shows signals generated by x and X along an orbit of the coupled system after a transient of 250 seconds starting from an initial data outside $\{x = X, y = Y, z = Z\}$. In the manuscript, it corresponds to transitions between interval of c values A→B→C. Interval B associated to *relaxation loss of one oscillator* is very narrow. The detailed transitions (not shown in this animation) between the above synchronization types involve complex changes in the phase portrait (canard explosion and cascade of bifurcations) that occur in exponentially small (w.r.t. ε) intervals of c values.

In intervals C and E of c values, the sequences of return times converge for both oscillators: the 25 green and 25 blue points materializing the successive return times for each oscillators cannot be distinguished. Moreover, the limit is the same for both oscillators. Hence, the sets of blue and green points coincide

and the blue points are hidden behind the green ones. These cases correspond to cases (c) and (e) of Fig. 4, respectively. It is also the case for subintervals of D for which the oscillators are perfectly synchronized (case (e) in Fig. 4) and generate a MMO orbit. A discrepancy between the return times occur for the other c values in interval D corresponding to almost-in-phase synchronization of MMO patterns (case (d) in Fig. 4) either periodic with a constant phase shift between two successive relaxation or more complex with numerous values of the phase-shifts (red dots). Above interval C, we have also plotted the half of the return time (dashed black line), which coincides precisely with the time shift between oscillators. This fact shows that the oscillators are in perfect antiphase for c values in interval C.

Note that for $c > 0$ the activity phases of the oscillators tend to facilitate each other, while for $c < 0$ the activation of one oscillator blocks the possibility of activation for the other one. Thus, we can naturally interpret $c > 0$ as mutual excitatory case, while $c < 0$ can be interpreted as mutual inhibitory case.

In the sequel, we formalize theoretically the repartition shown in this simulation and present dynamical explanations of the occurrence and properties of each behavior according to c value.

3. Theoretical analysis of the main behaviors repartition

The section is divided into three subsections. In subsection 3.1, we present a preliminary result about the impact of one oscillator onto the behavior of the other one. In subsection 3.2, we establish the main result of this work, where we obtain macroscopic intervals where the asymptotic behavior of system (12) is asymptotically stable. Finally, in subsection 3.3, we focus on the dependency of an asymptotic orbit period on the coupling gain parameter when the system displays antiphase synchronization. In particular, we prove that the frequency increases with the (negative) parameter c value.

3.1. Analysis of the impact of one 3D oscillator state upon the other one

In the following proposition, which is a preliminary result in order to prove the main result of this work in the next subsection, we discuss the effect of X on subsystem O_1, i.e., the impact of oscillator O_2 state upon oscillator O_1 transitory dynamics. Due to the symmetry between O_1 and O_2 in the 6D dynamics, the reverse situation is exactly the same one. When $c \neq 0$, the new $y-$nullcline is given by

$$\Pi_c \equiv \left\{ y = \frac{-(1+c)x - a_2 + cX}{a_1} =: r(x, X; c) \right\}, \tag{16}$$

and then, parameter c changes the $y-$nullcline in two different ways:

1. it changes the slope of plane Π_c;
2. it changes the position of plane Π_c, depending on the value of X.

In the sequel, we will refer to an X-dependent stable singular point of O_1 as a "stable quasi-equilibrium", since it is moving with the value of X. We use this notion to describe the motion of O_1 current point "following a stable quasi-equilibrium point" during a phase where it cannot experience a slow-fast transition due to the position of X-dependent Π_c. We use such notion since it enables a much easier description than discussing all the possible changes in the sign of the x, y and z dynamics that are not required for depicting O_1 qualitative behaviors.

Subsequently, we include a sketch of Proposition 1 proof, where we depict the special curves of the critical manifold S_b and S_h given in eqs. (9) and (10), respectively, and the X-dependent position of plane Π_c while X travels along phases I and IV of the limit cycle $\gamma_{\mu,\varepsilon}(t)$ of the uncoupled case. We emphasize that, in the figures, we represent these objects in the same (x, y)-plane, having in mind that they are located in the plane $z = z_b$ for $x < x_{on}$ and in the plane $z = z_h$ for $x > x_{on}$. For the sake of brevity, the remainder of the proof has been relegated to Appendix B. We recall that Phases I-IV have been defined at the end of subsection 2.1.

Proposition 1. *Consider system (12). Assume that, for $c = 0$, the values of the remainder parameters of the system are fixed so that each oscillator O_1 and O_2 admits the attractive MMO limit cycle $\gamma_{\mu,\varepsilon}(t)$. There exists $0 < \delta \ll 1$ (precisely δ of the same order as $|a_1|$) so that, for $|c| > \delta$, while O_2 current point $P_2 = (X, Y, Z)$ lies close to $S_l \cap \{X \in [x_{\min}, -x_f]\}$ or $S_r \cap \{X \in [x_f, x_{\max}]\}$, the motion of O_1 current point $P_1 = (x, y, z)$ under the impact of the coupling term $c(x - X)$ in the y-dynamics is the following.*

1. *Consider $c > \delta$.*
   (a) *While X increases from $x_{\min}$ to $-x_f$ (O_2 in phase I, P_2 is ε-close to S_l), P_1 follows a stable quasi-equilibrium point lying on S_l and moving rightwards. When this equilibrium passes through the lower fold, P_1 generates small oscillations and then reaches quickly S_r vicinity.*
   (b) *While X decreases from $x_{\max}$ to x_f (O_2 in phase IV, P_2 is ε-close to S_r), P_1 generates relaxation oscillations.*
2. *For $c < -\delta$.*
   (a) *While X increases from $x_{\min}$ to $-x_f$, P_1 either oscillates or follows a stable quasi-equilibrium point lying on S_r.*
   (b) *While X decreases from $x_{\max}$ to x_f, P_1 follows a stable equilibrium point lying on S_l.*

Sketch of the proof

For each oscillator, the $x-$nullcline is the critical manifold S given in eq. (4) and the $z-$nullcline is the sigmoidal surface Γ given in eq. (8). The $y-$nullcline is Π given in eq. (7) in the uncoupled case, and Π_c given in eq. (16) in the coupled case with coupling gain c. First, note that

$$\Pi \cap \Pi_c = \left\{ \left(X, -\frac{X + a_2}{a_1}, Z \right) \middle| \, X \in \mathbb{R}, Z \in \mathbb{R} \right\}$$

and in particular, for $X = -x_f$,

$$\Pi \cap \Pi_c \cap \{X = -x_f\} = \left\{ \left(-x_f, \frac{x_f - a_2}{a_1}, Z \right) \middle| \, Z \in \mathbb{R} \right\}. \tag{17}$$

There are four different possibilities:

1. If $c > 0$,
   (a) $X \in (x_{\min}, -x_f)$.
   (b) $X \in (x_f, x_{\max})$.
2. If $c < 0$,
   (a) $X \in (x_{\min}, -x_f)$.
   (b) $X \in (x_f, x_{\max})$.

We represent in Fig. 9 the dynamical configurations of the four cases, that give rise to the statements of the proposition. In particular, we depict the special curves of the critical manifold S_b and S_h given in eqs. (9) and (10), respectively, and the X-dependent position of plane Π_c while X travels along phases I and IV of the limit cycle $\gamma_{\mu,\varepsilon}(t)$ of the uncoupled case. The technical details that allow to finish the proof are included in Appendix B.

At this point, we are ready to study the different synchronization patterns generated by the interaction between both oscillators.

3.2. Repartition of the main behaviors according to the coupling gain.

We take advantage of the analysis in the preceding subsection for studying the synchronization patterns generated by the interaction between the coupled oscillators. The following theorem formalizes the macroscopic structure of the behavior repartition w.r.t. parameter c shown in Fig. 6 and the observations made in subsection 2.5.

Subsequently, we include a sketch of the proof of the Theorem. The most technical part of the proof has been relegated to Appendix C.

Theorem 3.1. *Consider system (12). Assume that when $c = 0$ the remainder parameters of the system are fixed so that O_1 and O_2 admit an attractive MMO limit cycle $\gamma_{\mu,\varepsilon}(t)$. There exist $0 < \delta_0, \delta_1, \ldots, \delta_5 \ll 1$, such that, for different initial conditions on each subsystem, the coupled system (12) displays the following synchronization patterns, depending on parameter c.*

1. *Case $c > \delta_0$ (regions D and E in Fig. 6). The two oscillators are in-phase locking or almost-in-phase synchronized. The MMOs persist under*

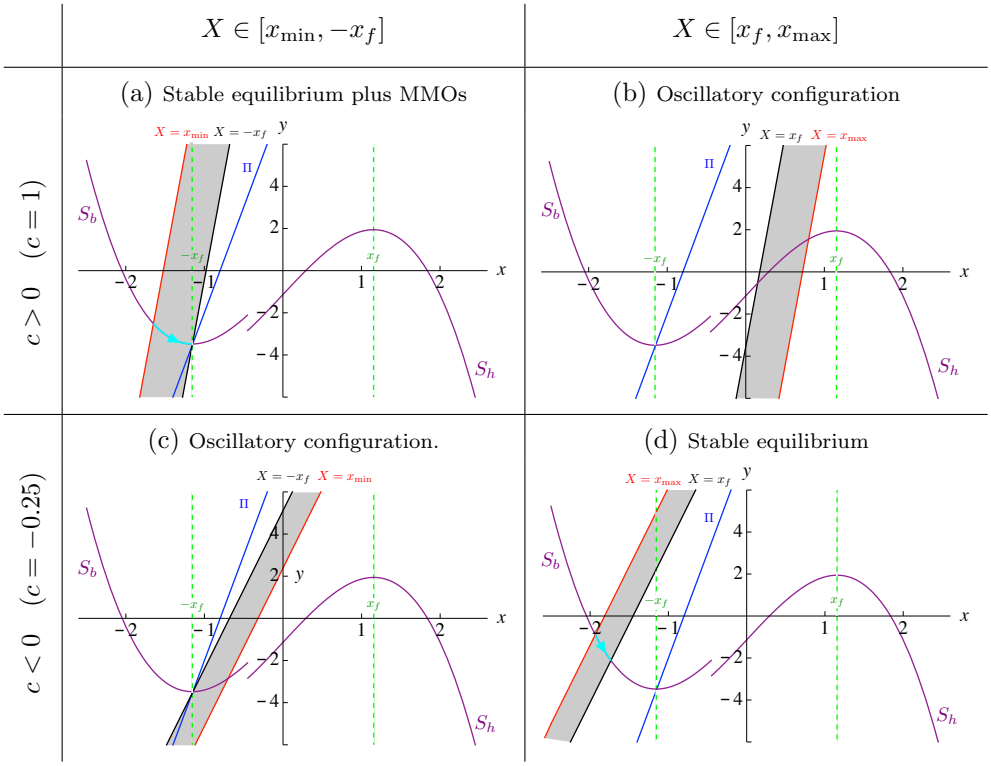

Figure 9: Projections of the nullclines of oscillator O_1 with parameter values given by 11 in different cases: $c > 0$ (top) and $c < 0$ (bottom), $X \in [x_{\min}, -x_f]$ (left) and $X \in [x_f, x_{\max}]$ (right). We represent in the same (x, y)-plane the two planes $z = z_b$ for $x < x_{on}$ and $z = z_h$ for $x > x_{on}$. In purple, the special curves of the critical manifold S_b and S_h given in eq. (9); in blue, plane Π corresponding to the uncoupled case; the grey area materializes the locus of plane Π_c for X increasing from $x_{\min}$ (red line) to $-x_f$ (black line) for (a) and (c), and for X decreasing from $x_{\max}$ (red line) to x_f (black line) for (b) and (d). The dashed green lines materialize the x-component of the folds $x = -x_f$ and $x = x_f$. In case (a) and (d), O_1 admits a stable equilibrium moving rightwards (cyan trajectories) while X decreases from $x_{\max}$ to x_f: in (a), this point eventually crosses the fold leading to small oscillations, while in (d) this point lies on the left sheet for any $X \in [x_f, x_{\max}]$. In case (b) and (c), O_1 is in oscillatory configuration since the X-dependent singular point always lies on the middle sheet S_m of S.

the coupling, i.e. each oscillator generates small oscillations close to the lower fold of their respective critical manifold.

2. *Case $c < -\delta_1$. We can distinguish three different subcases separated by the limit values $c^d < c^0 < 0$:*

(i) *For* $c \in (c^0 + \delta_2, -\delta_1)$, *(region C in Fig. 6), the oscillators* O_1 *and* O_2 *are in antiphase synchronization.*

(ii) *For* $c \in (c^d + \delta_4, c^0 - \delta_3)$ *occurs the relaxation loss of one oscillator, (region B in Fig. 6).*

(iii) *For* $c < c^d - \delta_5$, *the 6D system (12) admits a stable equilibrium point: there is a total oscillation death, (region A in Fig. 6).*

The MMOs disappear in the three cases, (see panels (a), (b) and (c) of Fig. 4). Moreover, c^0 *can be approximated by the only solution w.r.t.* $c \in [-1, 0]$ *of equation*

$$a_1 f(\tilde{x}) + (1 + c)\tilde{x} + a_2 - x_f c - a_1 \phi_f(z_b) = 0, \tag{18}$$

where

$$\tilde{x}(c, \mu) := \frac{1}{1 + c} \left(-a_1 f(x_f) - a_2 + c x_f + a_1 \phi_f(z_h) \right), \tag{19}$$

and c^d *can be approximated as the only real solution w.r.t.* c *of equation*

$$a_1 f(\hat{x}) + (1 + c)\hat{x} + a_2 - x_f c - a_1 \phi_f(z_b) = 0, \tag{20}$$

where

$$\hat{x}(c, \mu) := \frac{1}{c} \left[(1 + c)x_f + a_1 \left(f(x_f) - \phi_f(z_h) \right) + a_2 \right]. \tag{21}$$

Sketch of the proof.

The proof is based on joint slow-fast dissections taking into account that both oscillators are slow-fast systems and, therefore, any kind of oscillatory patterns of the 6D system is constituted by slow motions of P_1 and P_2 close to S_l and S_r, fast motions from the folds to the opposite stable branch, and occasionally small oscillations around the lower fold. Hence, except in the case of total oscillation death, during the slow motions along the 6D system orbits, x (resp., X) either increases between values ε-close to $x_{\min}$ and $-x_f$ or decreases between values ε-close to $x_{\max}$ and x_f. Depending on the value of c, using the results of Proposition 1, we verify for each case if the bidirectional conditions on O_1 and O_2 are fulfilled along the slow motions to produce the sequence of

active phase, silent phase and small oscillations of O_1 and O_2 associated with each synchronization feature (cases (a) to (e) of Fig. 4). We have relegated to Appendix C the detailed proof of statements 1 and 2 of the Theorem, and we include here the approximations of c^0 and c^d.

Recall that we denote $P_1 = (x, y, z)$ and $P_2 = (X, Y, Z)$ the current points of O_1 and O_2, respectively, along a given orbit of system (12) coupling O_1 and O_2. We know that *total oscillation death* occurs if both oscillators reach their respective stable equilibrium point, each of them lying on a different sheet (left or right) of the critical manifold. Without loss of generality, we focus on the case where the equilibrium point of O_1 lies on S_l, bearing in mind that the other case is exactly symmetric and arises for the same value of c. Since there exists a stable equilibrium point of O_1 on S_l for every $c < -\delta_1$ when $X > 0$, (see Fig. 9 (d)), we search for the value of c such that there exists also a stable equilibrium point of O_2 on S_r, preventing the current point from heading towards S_l. Hence, we can approximate the value c^d by considering the following limit case: for P_2 coinciding with the upper fold $\mathcal{F}^+$ of the special curve S^h, the equilibrium point of O_1 on the left sheet is such that the equilibrium point of O_2 is located exactly at the upper fold. Such condition is expressed by the following system of equations that the x-component of P_1 should fulfill.

$$\begin{cases} g_1(x, x_f; c) = 0, \\ g_2(x, x_f; c) = 0, \end{cases} \tag{22}$$

where

$$\begin{cases} g_1(x, X; c) = f(x) - \phi_f(z_b) - r(x, X; c), \\ g_2(x, X; c) = f(X) - \phi_f(z_h) - r(X, x; c), \end{cases} \tag{23}$$

with $r(x, X; c)$ given by eq. (16). System (22) writes

$$\begin{cases} a_1 f(x) + (1 + c)x + a_2 - cx_f - a_1\phi_f(z_b) = 0, \\ a_1 f(x_f) + (1 + c)x_f + a_2 - cx - a_1\phi_f(z_h) = 0. \end{cases} \tag{24}$$

The second equation of (24) is linear in x, hence for $c \neq 0$, we can express x as a function $\hat{x}(c, \mu)$ leading to statement (21) of the theorem. By substitution in

the first equation of (24), we obtain equation (20), which provides the roots of a polynomial function of degree 3 in $1/c$. For $|a_1|$ small enough, the equation admits only one real solution c^d.

We now consider the limit case between antiphase synchronization and relaxation loss for one oscillator, and search for an approximation of c^0 at order 0 w.r.t. ε. With this aim, we consider the fast motions of the current points to be instantaneous jumps from a fold to the opposite sheet of the critical manifold. Along an orbit in the case of relaxation loss of one oscillator (O_1 to fix the ideas), one of the current points (P_1) remains stuck on the left sheet, following the equilibrium point of O_1 driven by X, while the other one (P_2) follows a relaxation cycle. Hence, the sign of $x - X$ should not change along the whole orbit and, consequently, neither the sign of $y - Y$. On the contrary, along an orbit of the antiphase synchronization case, P_1 and P_2 alternatively undergo relaxation: when P_2 arrives at the upper fold and jumps on the left sheet of the critical manifold, P_1 is close to the moving equilibrium point of O_1 on the left sheet that shall already be below (i.e. admit a lower y-component than P_1), so that P_1 will be ahead of P_2 and subsequently undergoes relaxation. Hence, at order 0 w.r.t. ε, c^0 corresponds to the configuration of the nullclines shown in Figure 10: we look for c such that, for $X = x_f$ (P_2 is above the upper fold), the $y-$nullcline of O_1 intersects the x and $z-$nullclines at the height y of the upper fold. Therefore, c^0 can be approximated by the solution of

$$\begin{cases} g_1(x, x_f; c) = 0, \\ f(x_f) - \phi_f(z_h) = r(x, x_f; c), \end{cases} \tag{25}$$

where $g_1(x, X; c)$ is defined by eq. (23) and $r(x, X; c)$ by eq. (16). System (25) writes

$$\begin{cases} a_1 f(x) + (1 + c)x + a_2 - cx_f - a_1\phi_f(z_b) = 0, \\ a_1 f(x_f) + (1 + c)x + a_2 - cx_f - a_1\phi_f(z_h) = 0. \end{cases} \tag{26}$$

The second equation is linear in x, so for $c \neq -1$, we can find $x = \tilde{x}(c)$ given by (19) and substitute in the first equation of (26). Resulting equation (18) gives the roots of a polynomial function in $\tilde{c} = 1/(c + 1)$ of degree 3. For a_1 small

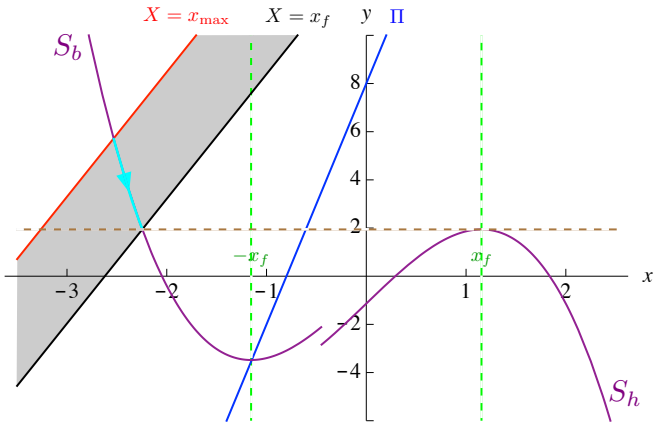

Figure 10: Projections of the nullclines of oscillator O_1 with parameter values given by 11, $c = c^0 \approx -0.482$ and X decreasing from $x_{\max}$ to x_f. We represent in the same plane the two planes $z = z_b$ for $x < x_{on}$ and $z = z_h$ for $x > x_{on}$. In purple, the special curves of the critical manifold S_b and S_h given in eq. (9); in blue, plane Π corresponding to the uncoupled case; the grey area materialize the locus of plane Π_c for X between $x_{\max}$ (red line) and $X = x_f$ (black line). Considering X decreasing between these values, O_1 current point stays close to the stable singular point, which follows the cyan trajectory. The dashed green lines materialize the x-component of the folds $x = -x_f$ and $x = x_f$ and in brown the fast fibers corresponding to the upper fold $\mathcal{F}^+$. The c value corresponding to the transition between antiphase synchronization and loss of relaxation of one oscillator is approximated by the c value such that O_1 singular point for $X = x_f$ has the same y-component as the upper fold (black, purple and dashed brown lines intersect at the same point).

enough, the equation possesses only one solution greater than one for $\tilde{c}$, that we can find explicitly and note $\tilde{c}^0$. Finally, $c^0 = 1/\tilde{c}^0 - 1$, concluding the proof.

Let us remark that, for the parameter values given by 11 and $\mu = 2.4$ used in the simulations along this section, we find from Theorem 3.1 the approximate values $c^d = -0.509$ and $c^0 = -0.482$, while we obtain $c^d = -0.509$ and $c^0 = -0.501$ from numerical simulations.

Now, we proceed to next subsection, where we analyze the frequency increase in the antiphasic case with respect to parameter c value.

3.3. Frequency increase with c in the antiphasic case

Remark first that the statement and the proof of case 2.(b) (antiphase synchronization) in Theorem 3.1 only describes the qualitative behavior of the orbits for $c \in [c^0 + \delta_2, -\delta_1]$, i.e. the alternation of active phase of each oscillator. In addition, from the symmetry of the system, i.e. the facts that the oscillators O_1 and O_2 are identical and the coupling is symmetric, we obtain directly, for each $c \in [c^0 + \delta_2, -\delta_1]$, the existence of a particular periodic orbit $(x(t), y(t), z(t), X(t), Y(t), Z(t))$ of period T such that $x(t + T/2) = X(t), y(t+T/2) = Y(t), z(t+T/2) = Z(t)$ for all t. In the sequel, we will refer to this particular orbit as the "perfect antiphase periodic orbit". However, either proving that this periodic orbit is a limit cycle (isolation) or that it is stable are very difficult problems to tackle theoretically for such system. Remark though that Fig. 6 shows numerically that, for a large interval of c values, the perfect antiphase orbit is actually an attractive limit cycle. Moreover, it shows that the oscillation frequency is increasing with c, i.e. the return time decreases while c increases, that is, $|c|$ decreases.

No matter the isolation and attractiveness of the perfect antiphase periodic orbit, in this section, we give an approximation of its period for small values of ε by neglecting the duration of the fast parts of the dynamics. We prove that this approximate period decreases while c increases and we provide a global upper bound of its partial derivative w.r.t. c.

We first give a synoptic view of the durations that will be computed in the following theorems by means of Figure 11. From the symmetry of perfect antiphase periodic orbit, the duration T_1 of the active phase during which $x > 0$ and $X < 0$ equals the duration of the active phase during which $x < 0$ and $X > 0$. Similarly, the duration T_2 of the recovery phase during which $x < X < 0$ equals the duration of the recovery phase during which $X < x < 0$. The global period is then twice the sum of the active phase and the recovery phase durations, hence $2(T_1 + T_2)$.

For the sake of simplicity, in the following, we express both approximations T_1 and T_2 of the active phase and recovery phase durations using integrals

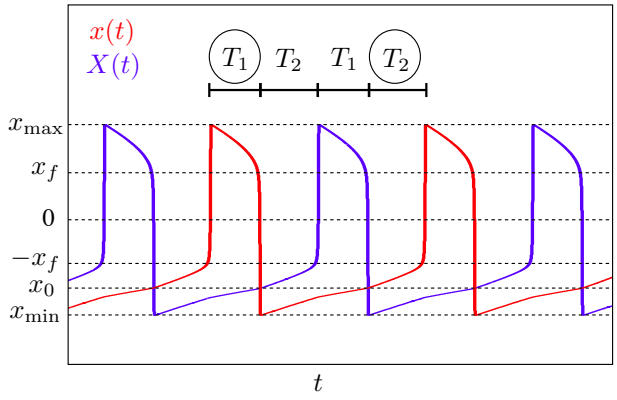

Figure 11: Decomposition of the global period of the perfect antiphase periodic orbit into two active phase durations (T_1) and two recovery phase durations (T_2).

parameterized by variable x from $x_{\max}$ to x_f and from x_0 to $-x_f$ respectively, where x_0 is the x value of the equilibrium point of O_1 at the end of the O_2 active phase. In other words, we compute the approximate durations in the cases corresponding to the situations associated with circled T_1 and T_2 in Figure 11.

We recall that, during the active phase, the current point $P_1 = (x, y, z)$ of O_1 follows the right slow manifold ε-close to $y = f(x) - \phi_f(z), x > x_f$, for the Hausdorff distance. Along the corresponding trajectory, x decreases from a maximal value $x_{\max}$ to the right fold value x_f, and the state variables of the second oscillator remains close to a stable equilibrium point, slowly moving with the value of x. Once x becomes less than x_f, the first oscillator experiences a fast motion of negligible duration before the beginning of the subsequent recovery phase. The following theorem takes advantage of reductions to the slow manifolds and quasi-stationary approximations to state an integral expression for the duration of P_1 slow motion (under the impact of the bidirectional coupling) when x goes from $x_{\max}$ to x_f.

Theorem 3.2. *Assume the hypotheses of Theorem 3.1, 2.(i), $c \in (c^0 + \delta_2, -\delta_1)$, leading to antiphase synchronization between oscillators. Consider a parameterization $(x(t), y(t), z(t), X(t), Y(t), Z(t))$ of the perfect antiphase periodic orbit $\mathcal{C}(c, \varepsilon)$. The duration of O_1 (resp. O_2) active phase, i.e. the time spent by P_1*

(resp. P_2) close to S_r during one cycle, can be approximated at the first order in ε by $T_1(c,\varepsilon) + O(1)$ with

$$T_1(c,\varepsilon) = \frac{1}{\varepsilon\tau}\left(\int_{x_{\max}}^{x_f} \frac{f'(x) + \frac{\partial \psi_r}{\partial x}(x,z,\varepsilon)}{a_1 f(x) + (1+c)x - c\tilde{X}(x,c,\varepsilon) + k_r(x,z,\varepsilon)} dx\right), \quad (27)$$

where

$$\tilde{X}(x,c,\varepsilon) = X_{eq}(x,c,\varepsilon) + O(\varepsilon), \quad (28)$$

$X_{eq}(x,c,\varepsilon)$ denotes the X component of O_2 equilibrium point moving with x and lying on the left sheet of the critical manifold,

$$k_r(x,z,\varepsilon) = a_2 + a_1\psi_r(x,z,\varepsilon) - a_1\phi_f(z) - \left(\phi_f'(z) + \frac{\partial \psi_r}{\partial z}(x,z,\varepsilon)\right)\left(\phi_r(x) - \frac{z - z_b}{\tau_z}\right), \quad (29)$$

with $\phi_f(x)$ given by eq. (2), $\phi_r(x)$ given by eq. (3), and ψ_r is a differentiable function defined on

$$(x_f, x_{\max}) \times I_z^r \times (0, \varepsilon_0),$$

with I_z^r the interval of z values along $\mathcal{C}(c,\varepsilon)$ while $x \in (x_f, x_{\max})$, such that

$$\exists \xi_r(\varepsilon) = O(\varepsilon^{2/3}), \text{such that, } \forall (x,z) \in (x_f, x_{\max}) \times I_z^r, \quad |\psi_r(x,z,\varepsilon)| < \xi_r(\varepsilon). \quad (30)$$

595 *Sketch of the proof.*

The detailed proof of Theorem 3.2 is available in Appendix D. After rescaling the system, we use the symmetry of the system in the antiphase regime for giving an approximation of the time that the current point P_1 of O_1 spends along S_r during one cycle. We parametrize the corresponding part of the cycle
600 by (x,z) and use an implicit expression of the slow manifold $S_{r,\varepsilon}$ together with the differentiable property of this parameterization. From the reduction of the X-dependent O_1 flow to the slow manifold, we obtain a formal expression of T_1 corresponding to eq. (27).

Theorem 3.3. *With the same hypotheses and notations as in Theorem 3.2, the recovery time of the perfect antiphase periodic orbit can be approximated at first*

order in ε *by* $T_2(c,\varepsilon)+O(1)$ *where*

$$T_2(c,\varepsilon)=\frac{1}{\varepsilon\tau}\left(\int_{x_0(c)}^{-x_f}\frac{f'(x)+\frac{\partial\psi_l}{\partial x}(x,z,\varepsilon)}{a_1f(x)+(1+c)x-c\hat{X}(x,c,\varepsilon)+k_l(x,z,\varepsilon)}dx\right), \quad (31)$$

$x_0(c)$ *is the* x *value of the equilibrium point of* O_1 *at the end of the* O_2 *active phase, i.e. the unique solution for* $x<-x_f$ *of equation*

$$a_1f(x)+(1+c)x+a_2-cx_f-a_1\phi_f(z_b)=0, \quad (32)$$

function $\hat{X}(x,c,\varepsilon)$ *is the parameterization of the* X *value along the part of* $\mathcal{C}(c,\varepsilon)$ *while* $x\in(x_{\min},-x_f)$,

$$k_l(x,z,\varepsilon)=a_2+a_1\psi_l(x,z,\varepsilon) - a_1\phi_f(z)-\left(\phi_f'(z)+\frac{\partial\psi_l}{\partial z}(x,z,\varepsilon)\right)\left(\phi_r(x)-\frac{z-z_b}{\tau_z}\right),$$

with $\phi_r(x)$ *given in (2), and* ψ_l *is a differentiable function defined on*

$$(x_{\min},-x_f)\times I_z^l\times(0,\varepsilon_0),$$

with I_z^l *the* $z-$*path while* $x\in(x_{\min},-x_f)$ *along* $\mathcal{C}(c,\varepsilon)$, *such that*

$$\exists\xi_l(\varepsilon)=O(\varepsilon^{2/3}),\ such\ that,\forall(x,z)\in(x_{\min},-x_f)\times I_z^l,\quad |\psi_l(x,z,\varepsilon)|<\xi_l(\varepsilon). \quad (33)$$

Sketch of the proof.

The detailed proof of Theorem 3.3 is available in Appendix E. It is mainly based on the same idea as the proof Theorem 3.2: we give an approximation of the time that the current point P_1 of O_1 spends along S_l during one cycle. Yet an important difference consists in the parameterization $\hat{X}$ of X path during the silent phase, which naturally depends on x. After the reduction of the X-dependent O_1 flow to the left slow manifold, we keep this dependency in the formal expression of T_2 corresponding to eq. (31). Nevertheless, this does not impact the differentiability properties of the implicit functions introduced in the statement.

In the subsequent Theorem 3.4, we prove that T_1 and T_2 decrease as c increases in $[c^0+\delta,-\delta]$.

Theorem 3.4. *For $c \in [c^0 + \delta_2, -\delta_1]$ and ε small enough,*

$$\frac{\partial T_1}{\partial c}(c, \varepsilon) < 0 \quad \textit{and} \quad \frac{\partial T_2}{\partial c}(c, \varepsilon) < 0. \tag{34}$$

Consequently, the first order approximation in ε of the global period $2(T_1(c, \varepsilon) + T_2(c, \varepsilon))$ of the perfect antiphase periodic orbit, decreases while parameter c increases and the global oscillation frequency is increasing with c.

Sketch of the proof. The proof of Theorem 3.4 is available in Appendix F. We first prove a technical Lemma stating that $x_0(c)$ introduced in Theorem 3.3 (the x value of O_1 equilibrium point at the end of O_2 active phase) increases with c in the antiphase case. From Leibniz formula applied to the integral expression of T_1, we obtain easily $\frac{\partial T_1}{\partial c}(c, \varepsilon) < 0$. We use the same tool for T_2, yet the dependency on $\hat{X}$ results in the sum of two terms in the integral defining $\frac{\partial T_1}{\partial c}(c, \varepsilon)$. The proof is based on the fact that the integral of the term known to be negative (from the Lemma) compensates the integral of the other one, no matter its sign. This is proved by bounding this integrand by a positive function that we can explicitly integrate.

Remark that the decrease of the period can only be obtained for a subinterval of $(c^0, 0)$ from the above approach. This restriction results indirectly from the fact that the approximation of the trajectories durations using the reduction to the slow manifold only makes sense if we consider ε small enough. The result can be stated in two different ways depending on whether we fix ε or δ. The first one is stated in Theorem 3.4: we define a fixed value of δ from geometrical properties (independently from ε), then there exists $\varepsilon^* > 0$ such that for any $\varepsilon \in (0, \varepsilon^*]$, for any $c \in [c^0 + \delta_2, -\delta_1]$, inequalities (34) hold. A second way could be to consider a value of ε small but fixed, then there exists a non-empty interval $[c^0 + \delta_2, -\delta_1]$ of c values along which the period of the perfect antiphase periodic orbit decreases. This statement implicitly link the optimal (i.e. smallest) values of δ_1 and δ_2 with ε that would tend to 0 with ε. Yet it is important to note that the proofs given in Appendices are not designed to allows δ to tend to 0 with ε.

It is worth noticing that numerical simulations for a fixed value of ε show

an increase of the period for small (in absolute value) negative values of c. But, more interestingly, they also show an interval $[-\eta, 0]$, (with $\eta > 0$) of c values for which the behavior is chaotic. In the next section, we provide numerical simulations and discuss the transitions undergone by the system behavior induced by the passage of c value from one macroscopic interval mentioned in Theorem 3.1 to another one.

4. Insight into almost-in-phase synchronization of MMOs

In Theorem 3.1, we have described the different behaviors of system (12), depending on the value of parameter c, out of the small regions in grey in Fig. 6, where tangled bifurcations take place. This section focuses on these intervals as well as on the sequence of bifurcations occurring in $[0, c^p]$ where the MMOs play an essential role.

This section is divided into two subsections. In the first one, we focus on the complex cascade of bifurcations for medium excitatory coupling. The second one is devoted to the chaotic behaviors observed for weak inhibitory and excitatory coupling.

4.1. Complex cascade of bifurcations for medium excitatory coupling

In the first item of Theorem 3.1, we have proven the qualitative property of almost-in-phase synchronization of the two coupled oscillators O_1 and O_2 resulting in MMO patterns for $c > 0$. Nevertheless, the existence of an attractive periodic orbit of the whole coupled system and the precise link between the value of c and the shift between the two oscillator patterns come under the theoretical study of the synchronization of MMOs, which remains a major and highly challenging problem. As a matter of fact, a large panel of complex bifurcations appears w.r.t. c in the case of weak excitatory coupling. In this section, we illustrate the high complexity of the bifurcation cascades occurring for $c \in [0, c^p]$ using numerical simulations and discuss the associated types of transitions, in particular in terms of MMO signature.

Figure 12 shows return times, shifts and return values associated with the signals generated by O_1 and O_2 according to the value of $c \in [0, c^p]$. Return times and shifts are defined as explained at the beginning of section 2.5 and the same protocol has been used for the numerical simulations. Recall that we note $(x_c(t), y_c(t), z_c(t), X_c(t), Y_c(t), Z_c(t))$ the solution of the coupled system for a fixed value of c starting from an initial condition that does not belong to the subspace $\{x = X, y = Y, z = Z\}$. For this simulation, we have used a 10^{-4} step grid of interval $[0.1, 0.8]$ for c values and kept the 26 last values $(t_i^{x=0}(c))_{i=0}^{25}$ and $(t_i^{X=0}(c))_{i=0}^{25}$ out of a hundred. In addition to the return times and phase shifts, we have retrieved the value of the first variable of each oscillator at the times when the other oscillator crosses the section $\{x = 0\}$ (resp. $\{X = 0\}$), i.e. for each value of c and for $i = [0, 25] \cap \mathbb{N}$,

$$x_i^{X=0}(c) = x_c(t_i^{X=0}(c)), \tag{35}$$

$$X_i^{x=0}(c) = X_c(t_i^{x=0}(c)). \tag{36}$$

The two top panels of Figure 12 show, for each value of c, the 25 return times $T_i^{x=0}(c) = t_i^{x=0}(c) - t_{i-1}^{x=0}(c)$ (green points) and $T_i^{X=0}(c) = t_i^{X=0}(c) - t_{i-1}^{X=0}(c)$ (blue points) for $i = [1, 25] \cap \mathbb{N}$. For the sake of comparison between the two sequences, we have plotted both on each panel, with the green points on top of the blue ones in the first panel and the blue points on top of the green ones in the second panel. The middle panel shows, for each value of c on the grid, the 25 evaluated shifts between the oscillators $(\phi_i(c))_{i=1}^{25}$. Two bottom panels show the sequences of crossed return values $(x_i^{X=0}(c))_{i=1}^{25}$ (green points) and $(X_i^{x=0}(c))_{i=1}^{25}$ (blue points), respectively.

Once again, from Fig. 12, we can isolate macroscopic subintervals of interval $[0.1, 0.8]$ of c values for which the system admits an attractive asymptotic behavior. Due to the symmetry between O_1 and O_2 assumed in this study (same parameter values and symmetric coupling), we obtain direct information on the MMO signature (number of small oscillations) displayed by $x(t)$ and $X(t)$ in the two following cases.

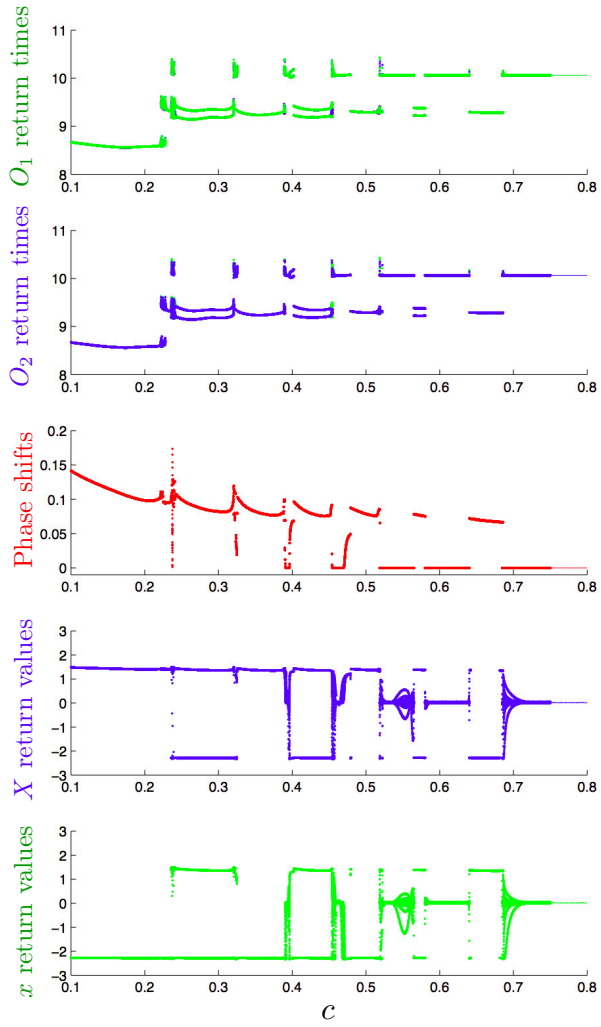

Figure 12: Return times, shifts and return values associated with the signals generated by O_1 and O_2 according to the value of $c \in [0, c^p]$. Two top panels: return times $(t_i^{x=0}(c))_{i=1}^{25}$ (green points) and $(t_i^{X=0}(c))_{i=1}^{25}$ (blue points), respectively, according to c. Both are plotted on each panel, with the green points on top of the blue ones in the first panel and the blue points on top of the green ones in the second panel. Middle panel: for each value of c on the grid, the 25 evaluated shifts between the oscillators $(\phi_i(c))_{i=1}^{25}$. Two bottom panels: sequences of crossed return values $(x_i^{X=0}(c))_{i=1}^{25}$ (green points) and $(X_i^{x=0}(c))_{i=1}^{25}$ (blue points), respectively.

- For a given value of c, the unicity of the X and x return points together with a single non vanishing shift value indicates that the asymptotic behavior is an almost-in-phase synchronization of a simple kind: there exists a stable limit cycle such that, along one period, each oscillator has a single activity phase.

- The existence of two (and only two) different return values for x and X, with a single phase shift value, corresponds to an attractive limit cycle such that, along one period, each oscillator has two activity phases. In that case, if O_1 begins an activity phase just before O_2, this activity phase is preceded by n small oscillations for O_1 and $n+1$ for O_2. Then, just before the subsequent activity phase, O_2 and O_1 display n and $n+1$ small oscillations, implying that O_2 becomes active slightly ahead of O_1.

In addition, chaotic behaviors arise when a large amount of different return values and phase shifts are recorded.

We can isolate four patterns of bifurcation cascades occurring in the transition between the two "simple" cases mentioned above: they are emphasized and numbered from 1 to 4 in 5 zooms on small intervals of c values included in $[0, c^p]$ shown in Fig. 13. Due to the symmetry between the oscillators, return value 0 has a particular place in the structure of the bifurcation diagram: it is associated with a perfect in-phase synchronization between the two oscillators, as shown by the associated vanishing phase shift. Yet, for neighboring values of c, cascades of period doubling bifurcation occur. Such a cascade implies a route to chaos if an infinite number of period doubling occur in a compact interval of c values. It is worth noticing that, along such a cascade, the return value of each oscillator from one quasi-period to the subsequent one is necessarily non zero. Yet the return value corresponds to a fast dynamics of the oscillator. Consequently, the phase shifts remain extremely close to 0.

Consider a starting c value leading to in-phase synchronization associated with a limit cycle of period T. We describe below the four types of transitions numbered from 1 to 4 observed in the simulation shown in Fig. 13 and refer to

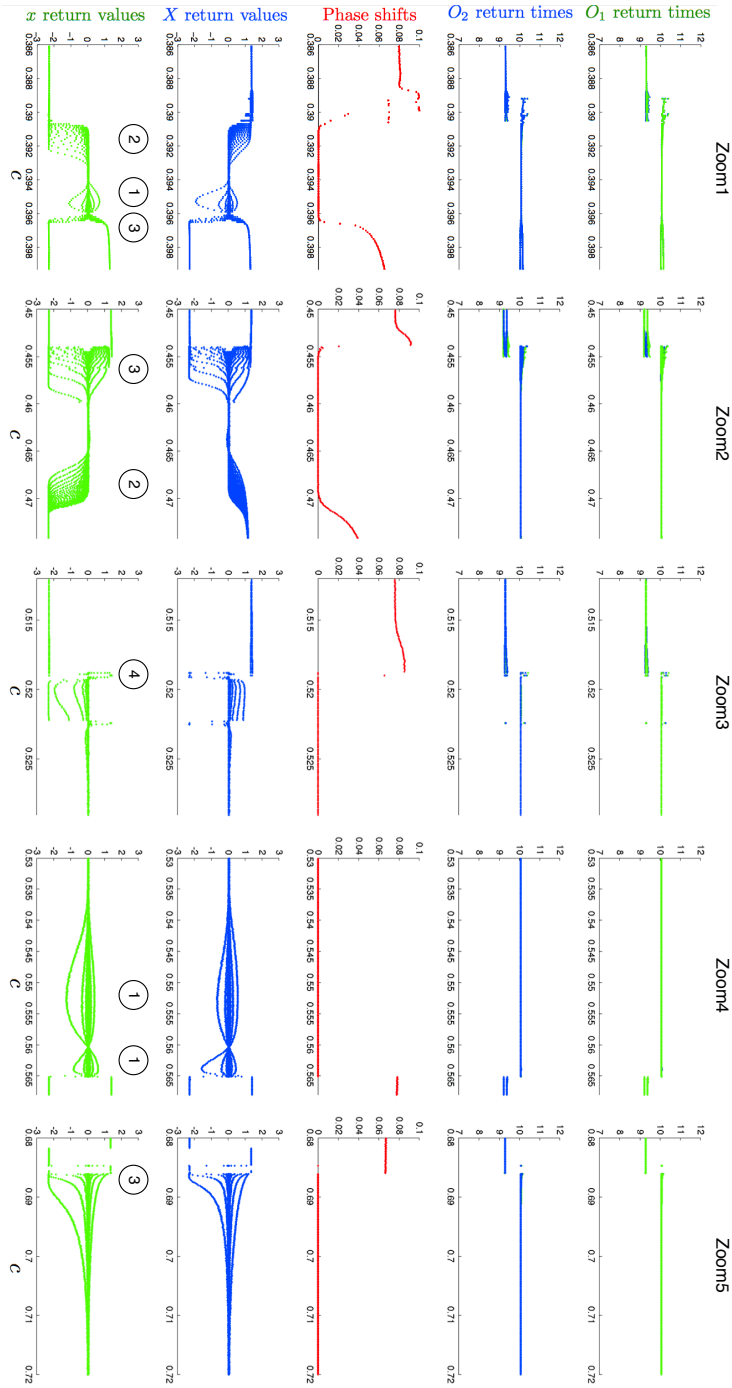

Figure 13: Magnified views of bifurcations in the transition from the cases of existence of an attractive limit cycle to chaotic behaviors.

Zoom1 to Zoom 5 for locating the phenomena.

1. Finite period doubling cascade: it resumes by an inverse process and leads to recover a similar orbit as the initial one (both oscillators return values close to 0). Such back and forth cascade is exemplified in Fig. 13 for $c \in [0.394, 0.396]$ (in Zoom1), for $c \in [0.535, 0.56]$, and for $c \in [0.56, 0.565]$ (both in Zoom4).

2. Infinite period doubling cascade: it results in chaotic dynamics for a small interval of c values, and leads to a limit cycle of period close to T. Such transition occurs, for instance, for c decreasing from 0.394 to 0.388 (Zoom1) and for c increasing from 0.465 to 0.475 (Zoom2). Note that the phase shift admits a unique value that is rather small, which evidences almost-in-phase synchronization. The resulting limit cycle is characterized by a single return value for one oscillator, greater than x_f, while the single return value of the other oscillator is lower than $-x_f$: the same oscillator is always ahead of the other one, i.e. if O_1 activates before O_2 at a certain time, O_1 always activates first afterwards. The whole transition consists in the addition of one small oscillation in the MMO generated by both oscillators (signature transition from 1^s to 1^{s+1}).

3. Infinite period doubling cascade resulting and priority exchange: it results in emergence of chaos and a subsequent structural re-stabilization of the dynamics and the existence of an attractive limit cycle. Yet, along this limit cycle, the oscillators exchange their priority from one activation to the subsequent one, i.e. if O_1 activates before O_2 at a certain time, O_2 activates first during the subsequent activation and the process repeats. Such transitions occur for instance for c increasing from 0.396 to 0.398 (in Zoom1) and for c decreasing from 0.46 to 0.45 (in Zoom2). In that case, the signature of the MMO generated by each oscillator is 1^s1^{s+1}.

4. Sudden appearance of chaos emerging from a long period limit cycle: this phenomenon occurs when decreasing c value from 0.52 to 0.515 (in

Zoom3). This transition is rather mysterious since the numerical simulations do not show evidence for a period doubling cascade. Nevertheless, it is clearly different from the three transitions mentioned above since the long period orbit includes a return value for one of the oscillator that is below $-x_f$. In other terms, another mechanism than the interactions between oscillators during their fast dynamics is involved in the emergence of the chaotic behavior.

Zoom5 in Fig. 13 ($c \in [0.68, 0.72]$) shows a transition of the third type, i.e. an infinite period doubling cascade resulting in a almost-in-phase synchronized orbit with alternation of priority between oscillators O_1 and O_2 after each active phase. We emphasize the simulation on this interval of c values around c^p since it corresponds to the stabilization of the symmetric orbit of the 6D system lying in $\{x = X, y = Y, z = Z\}$ into an attractive limit cycle for strengthened coupling gain (transition between intervals D and E in Fig. 6). Hence, for $c > c^p \approx 0.716$ corresponding to interval E, in-phase locking synchronization between oscillators O_1 and O_2 is the unique asymptotic behavior of the 6D system.

This relatively large variety of transitions in the dynamics highlights the complexity resulting from the interactions between the MMO generated by each oscillators. Despite almost-in phase or in-phase synchronization feature has been shown in Theorem 3.1 (case 1.), the changes in the fine structure of the phase portrait during these transitions are highly complex and their analysis necessitate more acute tools than geometric arguments based on singular perturbation theory.

4.2. Chaotic behaviors for weak inhibitory and excitatory coupling

Chaotic behaviors are expected for weak coupling, yet, in this subsection, we point out the clear difference in the emergence of chaos for excitatory versus inhibitory weak coupling.

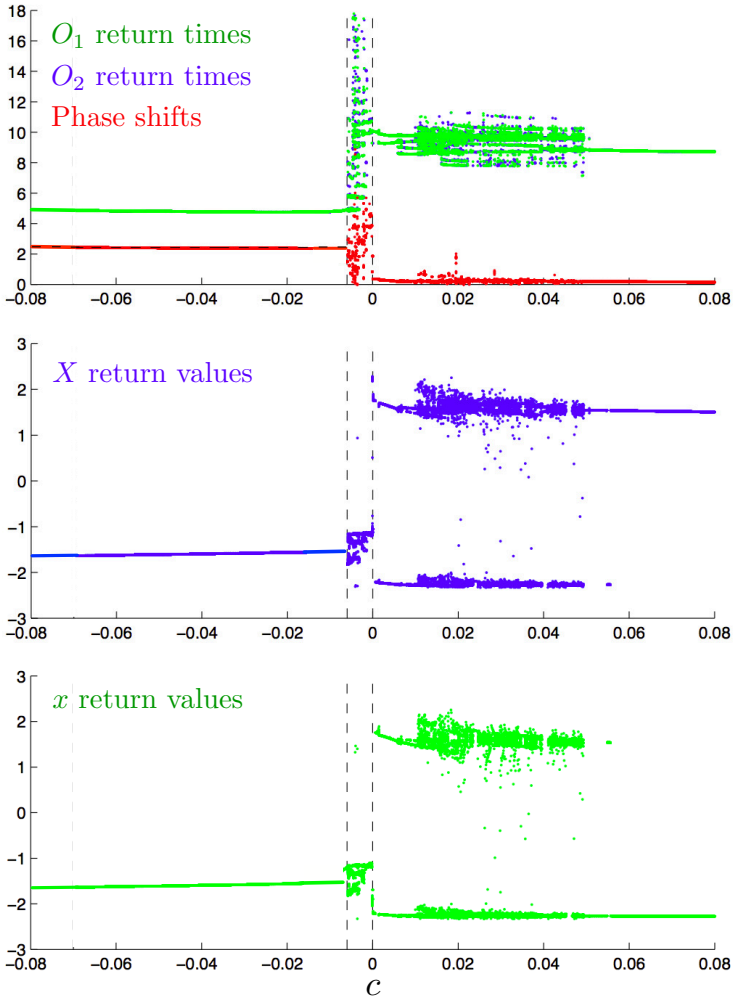

Figure 14: Return times and return values for $c \in [-0.08, 0.08]$ and 25 return values for each value of c in the 10^{-4} step grid.

Fig. 14 shows the return times and return values for c values in $[-0.08, 0.08]$ and, as before, 25 return values for each value of c in the 10^{-4} step grid for this interval. An animated view of the signals generated by x and X for varying c values together with the picture of Fig. 14 is provided as supplemental material (see animated Fig. 15).

For c increasing along $[-0.08, 0]$, the oscillators are first in perfect antiphase synchronization, and, from a precise value c^{chaos} of c up to 0, the model enters a chaotic behavior, evidenced in Fig. 14 by the large amount of different values of return times and return values for any fixed $c \in (c^{\text{chaos}}, 0)$. Note that the generated signals are anti-phasic in the sense that, along an orbit that does not belong to $\{x = X, y = Y, z = Z\}$, $x(t)$ and $X(t)$ are never positive at the same time.

On the contrary, weak excitatory coupling results in almost-in-phase synchronization between oscillators O_1 and O_2. Moreover, for an interval of c values bounded below by 0, the whole system admits a limit cycle along which the oscillators exchange their priority from one activation to the subsequent one. A period doubling cascade occurs for increasing c values, and therefore, chaotic behavior only emerges from a strictly positive value of c (around 0.02 in the simulation shown in Fig. 14).

5. Conclusions and future work

We have analyzed the synchronization of two identical 3D slow-fast systems generating MMOs under symmetric linear coupling according to the sign and strength of the coupling parameter. We have described the different synchronization patterns occurring in both the excitatory and inhibitory cases, corresponding to positive and negative values of coupling parameter c, respectively. Using geometric arguments and tools based on singular perturbation theory, we have proven that inhibition between cells only preserves sustained MMOs for weak coupling (small $|c|$ value), while excitatory coupling preserves MMO for any strength. We have also derived accurate approximations of the values of the

(Loading Video...)

Figure 15: Repartition of synchronization type between oscillator O_1 and O_2 for values of the coupling gain parameter from -0.06 to 0.08 with a $2\,10^{-4}$ step value. The top panel shows the 100 seconds signals generated by x and X along an orbit of the coupled system after a transient of 250 seconds starting from an initial data outside $\{x = X, y = Y, z = Z\}$. The bottom panel the sequences of 25 O_1 and O_2 return times (blue and green points), shifts (red points), half return times in case of antiphase synchronization (dashed black line). We refer to Fig. 14 in the manuscript for extended explanation. The moving vertical red bar materializes the c value corresponding to the associated frame of the top panel.

coupling gain parameter c separating the main behaviors of the system. Using reductions of slow parts of the orbit to the slow manifold, we have derived an integral expression of a $O(\varepsilon)$ approximation of the period in case of anti-phasic synchronization. We have used this approximation for proving that the frequency decreases when the strength of the inhibitory coupling increases, that is, $|c|$ decreases. Finally, we have stressed the various transitions occurring in case of medium excitation between cells, leading to (almost-)in-phase synchronization. Basing ourselves on numerical simulations on a fine grid of c values, we have identified period-doubling cascades of periodic orbits and interpreted the changes in the MMO signature along such cascades. This last part of the study is related to the problematic of MMO synchronization that is known to be tremendously difficult to tackle theoretically.

This study leads to different conclusions depending on the scale at which we consider the model. Considering that each 3D oscillator represents an individual cell following MMOs in its dynamical behavior, this study proves that strong enough coupling leads to in-phase synchronization between cells. Hence, such system can also be interpreted as an idealized model of two clusters of neurons, with excitatory coupling within each cluster and strong enough for the cells to be in-phase synchronized. From this viewpoint, this study is a first step for understanding the impact of inhibition or weak excitation on model of clustered cells in (at least) two different contexts. On the one hand, the inhibition case finds a direct application in the study of motoneurons that are often organized as two clusters (ipsi- versus contra-lateral side of the spinal chord). The role of inhibition between the two clusters, that is suggested by experimental data [1], is central leading to different reactions of the low motor system compartment to external stimulus. On the other hand, intracellular calcium concentrations have been recorded in cultured cells and these data (that we have used originally for fitting the single cell model [4]) evidenced the role of the synchronization of calcium oscillations in the GnRH secretion. The medium excitation case of the present study can be used for understanding the transition from synchronized to desynchronized behaviors of neurons.

Several perspectives of research are open by the results of the present study: we evoke the two most natural ones. The first question is related to the fine characterization of the transition between orbits of different periods and signatures in the almost-in-phase synchronization case. Different analyses should be performed depending on the type of transitions shown and discussed in Section 4. Note that geometric arguments are no longer sufficient to understand the fine mechanisms of period-doubling cascades (finite or infinite) and the precise properties of the MMO orbits (period, signature, asymptotic stability). The second natural extension consists in considering (at least weak) heterogeneity between cells, i.e. (slightly) different values of the parameters. Indeed, the strong assumption that the two cells are identical has allowed us to benefit from the symmetry of the 6D system for performing theoretical analysis. A natural way to extend the study is to introduce heterogeneity in parameter values among cells and consider the system as a perturbation of the identical oscillator case. Away from the transition between qualitatively different behavior, the structural stability of the unperturbed vector field ensures that a hyperbolic limit cycle persists under small perturbation, *i.e.* in case of sufficiently weak heterogeneity between cells. In particular, a central question is to characterize the new synchronization types obtained with asymmetric coupling.

Acknowledgments

The authors would like to thank Frédérique Clément and Fabrizio de Vico Fallani (INRIA Paris Centre) for funding and helpful discussions about this study. The first author is now supported by VPPI-US and partially supported by grants P12-FQM-1658 and MTM2015-65608-P.

References

[1] F. D. V. Fallani, M. Corazzol, J. R. Sternberg, C. Wyart, M. Chavez, Hierarchy of neural organization in the embryonic spinal cord: Granger-

causality graph analysis of in vivo calcium imaging data, IEEE Transactions on Neural Systems and Rehabilitation Engineering 23 (3) (2015) 333–341.

[2] R. FitzHugh, Impulses and physiological states in theoretical models of nerve membrane, Biophysical Journal 1 (6) (1961) 445–466.

[3] J. Nagumo, S. Arimoto, S. Yoshizawa, An active pulse transmission line simulating nerve axon, Proceedings of the IRE 50 (10) (1962) 2061–2070.

[4] M. Krupa, A. Vidal, F. Clément, A network model of the periodic synchronization process in the dynamics of calcium concentration in GnRH neurons, The Journal of Mathematical Neuroscience 3 (1) (2013) 4.

[5] J. Bélair, P. Holmes, On linearly coupled relaxation oscillations, Quarterly of Applied Mathematics 42 (2) (1984) 193–219.

[6] S. A. Campbell, M. Waite, Multistability in coupled FitzHugh–Nagumo oscillators, Nonlinear Analysis: Theory, Methods & Applications 47 (2) (2001) 1093–1104.

[7] E. M. Izhikevich, Phase equations for relaxation oscillators, SIAM Journal on Applied Mathematics 60 (5) (2000) 1789–1804.

[8] E. Lee, D. Terman, Stable antiphase oscillations in a network of electrically coupled model neurons, SIAM Journal on Applied Dynamical Systems 12 (1) (2013) 1–27.

[9] E. Lee, D. Terman, Stability of antiphase oscillations in a network of inhibitory neurons, SIAM Journal on Applied Dynamical Systems 14 (1) (2015) 448–480.

[10] D. Storti, R. Rand, Dynamics of two strongly coupled relaxation oscillators, SIAM Journal on Applied Mathematics 46 (1) (1986) 56–67.

[11] D. Storti, R. H. Rand, A simplified model of coupled relaxation oscillators, International Journal of Non-Linear Mechanics 22 (4) (1987) 283–289.

[12] D. Terman, E. Lee, J. Rinzel, T. Bem, Stability of anti-phase and in-phase locking by electrical coupling but not fast inhibition alone, SIAM Journal on Applied Dynamical Systems 10 (3) (2011) 1127–1153.

[13] N. Kopell, G. Ermentrout, Mechanisms of phase-locking and frequency control in pairs of coupled neural oscillators, Handbook of Dynamical Systems 2 (2002) 3–54.

[14] N. Kopell, D. Somers, Anti-phase solutions in relaxation oscillators coupled through excitatory interactions, Journal of Mathematical Biology 33 (3) (1995) 261–280.

[15] D. Somers, N. Kopell, Rapid synchronization through fast threshold modulation, Biological cybernetics 68 (5) (1993) 393–407.

[16] D. Somers, N. Kopell, Waves and synchrony in networks of oscillators of relaxation and non-relaxation type, Physica D: Nonlinear Phenomena 89 (1-2) (1995) 169–183.

[17] J. Drover, J. Rubin, J. Su, B. Ermentrout, Analysis of a canard mechanism by which excitatory synaptic coupling can synchronize neurons at low firing frequencies, SIAM journal on applied mathematics 65 (1) (2004) 69–92.

[18] B. Ermentrout, M. Wechselberger, Canards, clusters, and synchronization in a weakly coupled interneuron model, SIAM Journal on Applied Dynamical Systems 8 (1) (2009) 253–278.

[19] E. K. Ersöz, M. Desroches, M. Krupa, F. Clément, Canard-mediated (de) synchronization in coupled phantom bursters, SIAM Journal on Applied Dynamical Systems 15 (1) (2016) 580–608.

[20] E. K. Ersöz, M. Desroches, M. Krupa, Synchronization of weakly coupled canard oscillators, Physica D: Nonlinear Phenomena 349 (2017) 46–61.

[21] H. G. Rotstein, R. Kuske, Localized and asynchronous patterns via canards in coupled calcium oscillators, Physica D: Nonlinear Phenomena 215 (1) (2006) 46–61.

[22] A. M. Zhabotinsky, H. G. Rotstein, I. R. Epstein, N. Kopell, A canard mechanism for localization in systems of globally coupled oscillators, SIAM Journal on Applied Mathematics 63 (6) (2003) 1998–2019.

[23] J. Best, A. Borisyuk, J. Rubin, D. Terman, M. Wechselberger, The dynamic range of bursting in a model respiratory pacemaker network, SIAM Journal on Applied Dynamical Systems 4 (4) (2005) 1107–1139.

[24] E. M. Izhikevich, Synchronization of elliptic bursters, SIAM review 43 (2) (2001) 315–344.

[25] K.-L. Roberts, J. E. Rubin, M. Wechselberger, Averaging, folded singularities, and torus canards: Explaining transitions between bursting and spiking in a coupled neuron model, SIAM Journal on Applied Dynamical Systems 14 (4) (2015) 1808–1844.

[26] A. Sherman, Anti-phase, asymmetric and aperiodic oscillations in excitable cells – I. coupled bursters, Bulletin of mathematical biology 56 (5) (1994) 811.

[27] K. Jahn, J. Grosskreutz, K. Haastert, E. Ziegler, F. Schlesinger, C. Grothe, R. Dengler, J. Bufler, Temporospatial coupling of networked synaptic activation of AMPA-type glutamate receptor channels and calcium transients in cultured motoneurons, Neuroscience 142 (4) (2006) 1019–1029.

[28] P. G. Haydon, GLIA: Listening and talking to the synapse, Nature Reviews Neuroscience 2 (3) (2001) 185.

[29] W. Vandenberghe, V. P. Bindokas, R. J. Miller, W. Robberecht, J. R. Brorson, Subcellular localization of calcium-permeable ampa receptors in spinal motoneurons, European Journal of Neuroscience 14 (2) (2001) 305–314.

[30] M. De Pittà, V. Volman, H. Berry, E. Ben-Jacob, A tale of two stories: astrocyte regulation of synaptic depression and facilitation, PLoS computational biology 7 (12) (2011) e1002293.

[31] D. Wang, A. Bordey, The astrocyte odyssey, Progress in neurobiology 86 (4) (2008) 342–367.

[32] D. Blackburn, S. Sargsyan, P. N. Monk, P. J. Shaw, Astrocyte function and role in motor neuron disease: a future therapeutic target?, Glia 57 (12) (2009) 1251–1264.

[33] M. R. Duchen, Mitochondria, calcium-dependent neuronal death and neurodegenerative disease, Pflügers Archiv-European Journal of Physiology 464 (1) (2012) 111–121.

[34] F. Clément, J.-P. Françoise, Mathematical modeling of the GnRH pulse and surge generator, SIAM Journal on Applied Dynamical Systems 6 (2) (2007) 441–456.

[35] F. Clément, A. Vidal, Foliation-based parameter tuning in a model of the GnRH pulse and surge generator, SIAM Journal on Applied Dynamical Systems 8 (4) (2009) 1591–1631.

[36] A. Vidal, F. Clement, A dynamical model for the control of the gonadotrophin-releasing hormone neurosecretory system, Journal of Neuroendocrinology 22 (12) (2010) 1251–1266.

[37] S. Fernández-García, M. Desroches, M. Krupa, F. Clément, A multiple time scale coupling of piecewise linear oscillators. application to a neuroendocrine system, SIAM Journal on Applied Dynamical Systems 14 (2) (2015) 643–673.

[38] M. Krupa, A. Vidal, M. Desroches, F. Clément, Mixed-mode oscillations in a multiple time scale phantom bursting system, SIAM Journal on Applied Dynamical Systems 11 (4) (2012) 1458–1498.

[39] E. Köksal Ersöz, A. Vidal, F. Clément, Coupled multiple timescale dynamics in populations of endocrine neurons: Pulsatile and surge patterns of GnRH secretion, SIAM Journal on Applied Dynamical Systems 17 (1) (2018) 1052–1090.

[40] B. Ermentrout, M. Pascal, B. Gutkin, The effects of spike frequency adaptation and negative feedback on the synchronization of neural oscillators, Neural Computation 13 (6) (2001) 1285–1310.

[41] N. Fenichel, Geometric singular perturbation theory for ordinary differential equations, Journal of differential equations 31 (1) (1979) 53–98.

[42] J. Guckenheimer, Singular hopf bifurcation in systems with two slow variables, SIAM Journal on Applied Dynamical Systems 7 (4) (2008) 1355–1377.

[43] M. Krupa, M. Wechselberger, Local analysis near a folded saddle-node singularity, Journal of Differential Equations 248 (12) (2010) 2841–2888.

[44] P. Szmolyan, M. Wechselberger, Relaxation oscillations in $\mathbb{R}^3$, Journal of Differential Equations 200 (1) (2004) 69–104.

[45] P. Szmolyan, M. Wechselberger, Canards in $\mathbb{R}^3$, Journal of Differential Equations 177 (2) (2001) 419–453.

[46] M. Wechselberger, Existence and bifurcation of canards in $\mathbb{R}^3$ in the case of a folded node, SIAM Journal on Applied Dynamical Systems 4 (1) (2005) 101–139.

[47] M. Brøns, M. Krupa, M. Wechselberger, Mixed mode oscillations due to the generalized canard phenomenon, Fields Institute Communications 49 (2006) 39–63.

[48] J. Guckenheimer, P. Meerkamp, Unfoldings of singular hopf bifurcation, SIAM Journal on Applied Dynamical Systems 11 (4) (2012) 1325–1359.

[49] M. Desroches, J. Guckenheimer, B. Krauskopf, C. Kuehn, H. M. Osinga, M. Wechselberger, Mixed-mode oscillations with multiple time scales, Siam Review 54 (2) (2012) 211–288.

Appendix A. Computation of folded sigularities

Here we compute the folded singularities of system (1) [42, 43, 45, 47, 48, 46]. First, we consider the new time variable $s = \tau t$, and obtain the rescaled system

$$\begin{cases} \dot{x} = -y + f(x) - \phi_f(z), \\ \dot{y} = \varepsilon(x + a_1 y + a_2), \\ \dot{z} = \varepsilon \left(\phi_r(x) - \dfrac{z - z_b}{\tau_z} \right). \end{cases}$$

The associated reduced problem is given by

$$\begin{cases} h(x, y, z) = 0, \\ \dot{y} = l_1(x, y), \\ \dot{z} = l_2(x, z), \end{cases} \tag{A.1}$$

where we have denoted

$$\begin{cases} h(x, y, z) = -y + f(x) - \phi_f(z), \\ l_1(x, y) = x + a_1 y + a_2, \\ l_2(x, z) = \phi_r(x) - \dfrac{z - z_b}{\tau_z}. \end{cases}$$

Now, the reduced problem (A.1) projected onto the $(x, z)-$plane is given by

$$\begin{pmatrix} -h_x \dot{x} \\ \dot{z} \end{pmatrix} = \begin{pmatrix} h_y l_1 + h_z l_2 \\ l_2 \end{pmatrix} \Big|_{y=f(x,z)},$$

where $f(x, z)$ defines the critical manifold S (see (4)). A time rescaling by function $-h_x$ drives us to the desingularized system

$$\begin{pmatrix} \dot{x} \\ \dot{z} \end{pmatrix} = \begin{pmatrix} h_y l_1 + h_z l_2 \\ -h_x l_2 \end{pmatrix} \Big|_{y=f(x,z)}. \tag{A.2}$$

It is known that folded singularities are fold points $\bar{\mathbf{p}} = (\bar{x}, f(\bar{x}) - \phi_f(\bar{z}), \bar{z})$ of the critical manifold such that

$$(h_y l_1 + h_z l_2) \Big|_{y=f(\bar{x})-\phi_f(\bar{z})} = 0. \tag{A.3}$$

Remember that the critical manifold has two fold lines $\mathcal{F}^-$ and $\mathcal{F}^+$ given in (5) and (6), respectively. Let us consider $\bar{x} = -x_f \in \mathcal{F}^-$, analogously one can analyze the case $\bar{x} \in \mathcal{F}^+$.

Eq. (A.3) for $\bar{x} = -x_f$ is linear in μ, so for every $\bar{z}$, there exists $\bar{\mu}(\bar{z})$ such that $(-x_f, \bar{z})$ is a folded singularity for the 3D system with $\mu = \bar{\mu}(\bar{z})$. The linearization of the desingularized system (A.2) around the singular points $(-x_f, \bar{z})$ provides the topological type of the singular fold. The determinant D, trace T and discriminant $\Lambda = T^2 - 4D$ are represented in Fig. A.16 as a function of $\bar{z}$. Hence, there is a folded node for $\bar{z} \in (0, 1.14093)$, a folded saddle

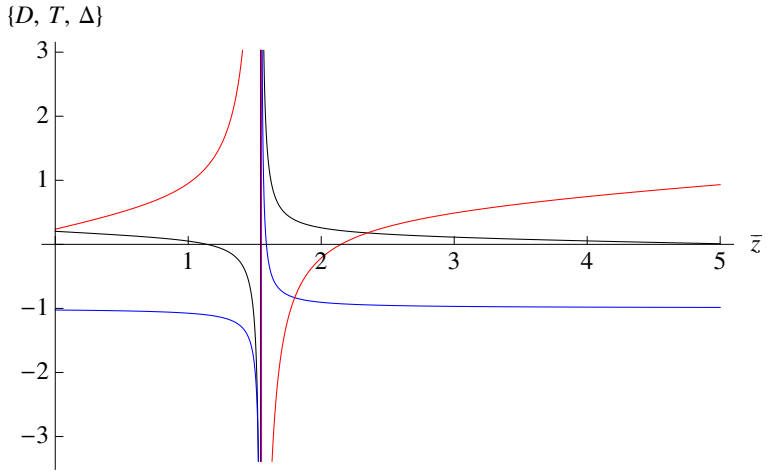

Figure A.16: Determinant D (black), trace T (blue) and discriminant $\Lambda = T^2 - 4D$ (red) of the linearization of the desingularized system around the singular folds $(-x_f, \bar{z})$. Parameter values are given by (11).

for $\bar{z} \in (1.14093, 1.54561)$ and a folded saddle-node for $\bar{z} = 1.14093$, which corresponds to $\mu = 2.51$. Moreover, it is possible to check that it corresponds to a real equilibrium of the full system (1), and then it is a folded saddle-node of type II [42, 43, 45, 47, 48, 46].

Appendix B. Technical details of the proof of Proposition 1.

Let us denote by x_u the first component of the only equilibrium point in the uncoupled case, which lies on the middle sheet of S but close to the lower fold. We proceed now through the different cases.

1. If $c > 0$, Π_c has a larger $x-$slope than Π. Moreover, if $X > 0$ (resp.

$X < 0$), the $y-$component of the intersection with $x = 0$ is smaller (resp. larger) than in the uncoupled case.

(a) Consider $X \in (x_{\min}, -x_f)$, i.e. O_2 in phase I. Taking into account that x_u is located in the middle sheet and Π_c has a larger $x-$slope than Π, together with relation (17), we have

$$\Pi_c \cap S \cap \Gamma \cap \{X = -x_f\} = \mathbf{q} := (x_q, y_q, z_q), \text{ with } x_q \in (-x_f, x_u).$$

Since x_q is close to the lower fold but still on the middle sheet, there exists a minimal value $\delta^{(0)} > 0$ such that, for $c > \delta^{(0)}$, $\Pi_c \cap S \cap \Gamma \cap \{X = x_{\min}\}$ lies on S_l, which implies the existence of a stable quasi-equilibrium point. Its x-component increases with X values (see Fig. 9 (a) for a global view and Fig. B.17 (a) for a zoom around the lower fold). Then, the current point $P_1 = (x, y, z)$ of O_1 is forced to follow a stable quasi-equilibrium that is moving rightwards, then to display small oscillations and finally to quickly reach S_r vicinity.

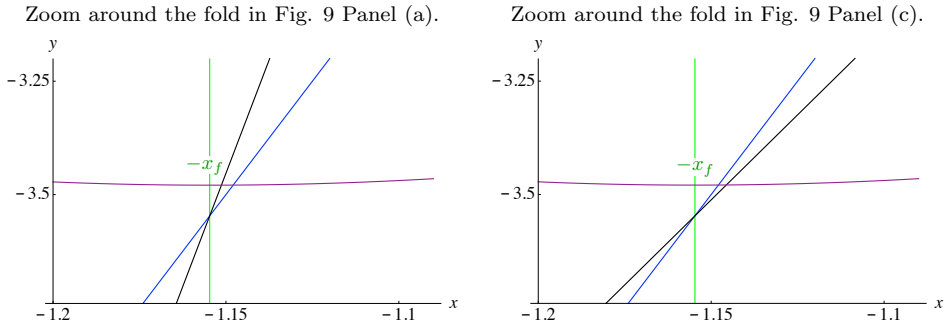

Figure B.17: Zoom around the lower folds in Fig. 9 (a) and (c), respectively. We represent in the same (x, y)-plane the two planes $z = z_b$ for $x < x_{on}$ and $z = z_h$ for $x > x_{on}$. In purple, the special curves of the critical manifold S_b and S_h given by (9); in blue, plane Π corresponding to the uncoupled case. The green lines materialize the x-component of the folds $x = -x_f$ and $x = x_f$.

(b) Consider $X \in (x_f, x_{\max})$, i.e. O_2 in phase IV. Then Π_c intersects the critical manifold of O_1 between the lower and upper fold, see Fig. 9 (b). Therefore,

O_2 undergoes relaxation oscillations.

2. If $c < 0$, Π_c has a lower $x-$slope than Π, which possibly gives rise to the existence of more than one quasi-equilibrium point for O_1. Moreover, if $X > 0$, the $y-$component of the intersection with $x = 0$ is larger than in the uncoupled case and if $X < 0$, it is smaller.

(a) Consider $X \in (x_{\min}, -x_f)$, i.e. O_2 in phase I. Bearing in mind that x_u is located on the middle sheet, Π_c has a lower $x-$slope than Π and from eq. (17), we have

$$\Pi_c \cap S \cap \Gamma \cap \{X = -x_f\} = \mathbf{v} := (x_v, y_v, z_v), \text{ with } x_v > x_u.$$

So, while $X \in (x_{\min}, -x_f)$, the possible quasi-equilibrium points of O_1 are on the right of the lower fold (see Fig. 9 (c) for a global view and Fig. B.17 (b) for a zoom around the lower fold). In this case, depending on the value of c, different possibilities may arise. Depending whether the $x-$slope of Π_c is smaller or larger than $f'(0)$ (the slope of the critical manifold at its inflection w.r.t the x direction), the system possesses either one, two or three equilibria. Moreover, function r defining Π_c in eq. (16) fulfills

$$\frac{\partial r}{\partial x}(0, X; c) = -\frac{c+1}{a_1}.$$

For $c \in [-1 - a_1 f'(0), 0)$ and $a_1 f'(0) > -1$, O_1 admits a single quasi-equilibrium point while $X \in (x_{\min}, -x_f)$, and if $c < -1 - a_1 f'(0)$, subsystem O_1 can have one, two, or three quasi-equilibrium points while $X \in (x_{\min}, -x_f)$. Hence, either a stable quasi-equilibrium point exists, lying on S_r, and P_1 follows it, or O_1 generates relaxation oscillations.

(b) Consider $X \in (x_f, x_{\max})$, i.e. O_2 in phase IV. There exists a minimal $\delta^{(1)} > 0$ such that, for $c < -\delta^{(1)}$, Π_c intersects S on its left sheet S_l (see Fig. 9 (d)). Then, in this case, P_1 follows the corresponding stable quasi-equilibrium moving rightwards as X decreases.

Finally, we take $\delta = \max\left(\delta^{(0)}, \delta^{(1)}\right)$.

Appendix C. Technical details of the proof of Theorem 3.1.

Recall that we denote $P_1 = (x, y, z)$ and $P_2 = (X, Y, Z)$ the current points of O_1 and O_2, respectively, along a given orbit of system (12) coupling O_1 and O_2. We consider $\delta_0 > \delta$ and $\delta_1 > \delta$, with δ defined in Proposition 1, and proceed case by case.

1. Case $c > \delta_0$. Consider, without loss of generality, that P_1 lies near S_l and far from its lower fold. From Proposition 1, case 1. (a), the quasi-equilibrium point of O_2 lies on S_l and is attractive (the nullclines of O_2 are as shown in Fig. 9 (a)), so that P_2 is forced to eventually reach a neighborhood of S_l. Then, each oscillator drives the y-nullcline of the other one rightwards, up to the vicinity of the lower fold. When one of the current points P_1 or P_2 arrives in the associated funnel, the quasi-equilibrium point of the other oscillator is located on the middle sheet, yet close to the lower fold (see the black lines shown in panel (a) of Fig. 9 and panel (a) of Fig. B.17). Hence, the bilateral coupling implies the generation of small oscillations.

To fix the idea in the following description, without loss of generality considering the symmetry between the oscillators, we assume that P_1 is ahead of P_2. When P_1 exits the funnel and heads towards S_r, the nullclines of O_2 are as shown in panel (b) of Fig. 9. From statement 1. (b) of Proposition 1, P_2 is also forced to head towards S_r almost instantaneously, since it is already located near the lower fold. Afterwards, both P_1 and P_2 climb up ε-close to S_r. Since the two oscillators are identical, they arrive almost at the same time in the upper fold vicinity. When P_1 comes back near the left sheet, P_2 experiences the same motion almost instantaneously (from statement 1. (a) of Proposition 1). The whole process repeats to generate the alternation of relaxation and small oscillations near the left folds for both oscillators. Hence, for $c > \delta_0$ the bilateral coupling tends to synchronize the oscillators, even if a small time shift may exist in the asymptotic behavior (see Fig 4 (d)).

2. Case $c < -\delta_1$. Consider, without loss of generality, that P_1 is ε-close S_l. Then, from statement 2.(a) of Proposition 1, O_2 either is in oscillatory regime

(the nullclines of O_2 are as shown in Fig. 9 (c)) or admits a stable quasi-equilibrium point on S_r (the nullclines of O_2 are as shown in panel (b) of Fig. C.18). When P_2 is ε-close to S_r, we know from statement 2.(b) of Proposition 1, that P_1 is forced to remain close to S_l. Now, we can distinguish three different cases, according to the limit values c^d and c^0, that will be computed subsequently. For now, we define c^d as the greatest (negative) value of c such that, for any $c < c^d$, two stable equilibria of the 6D system exist that are symmetric to each other with respect to the invariant plane $\{x = X, y = Y, z = Z\}$. One of them corresponds to a quasi-equilibrium of O_1 lying on S_l and a quasi-equilibrium of O_2 lying on S_r; the other one corresponds to the symmetric situation. We also define c^0 such that, for $X = x_f$ (P_2 above the upper fold), the $y-$nullcline of O_1 intersects the x and $z-$nullclines at the height y of the upper fold. Obviously, we have $c^d < c^0 < 0$.

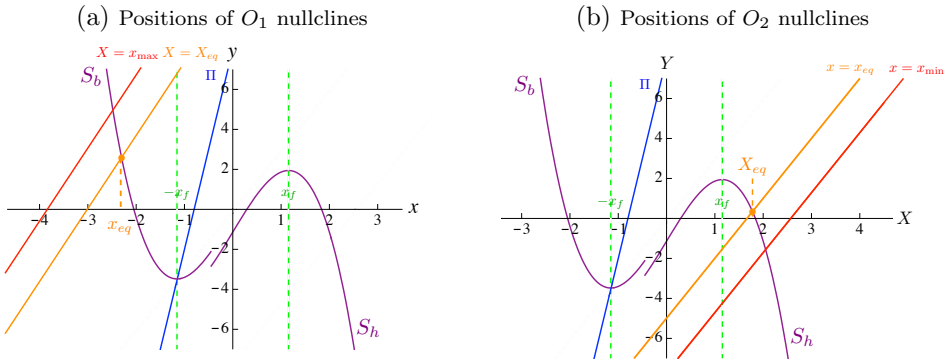

Figure C.18: Projections of the nullclines of oscillators O_1 (panel (a)) and O_2 (panel (b)) with parameter values given by 11 and $c = -0.7 < c^d$. We represent in the same plane the two planes $z = z_b$ for $x < x_{on}$ and $z = z_h$ for $x > x_{on}$. In purple, the special curves of the critical manifold S_b and S_h given in eq. (9); in blue, the plane Π (uncoupled case); in red, y-nullcline for $X = x_{\max}$ (panel (a)) and the Y-nullcline for $x = x_{\min}$ (panel (b)); in orange, the y and Y-nullclines for $x = x_{eq}$ and $X = X_{eq}$ corresponding to the stable quasi-equilibrium point of the coupled system. We also represent in green the lines $x = -x_f$ and $x = x_f$.

(i) For $c \in (c^0 + \delta_2, -\delta_1)$, the nullclines of O_1 when P_2 comes back near S_l are represented in panel (d) of Fig. 9. Thus, when P_2 approaches the upper

fold, P_1 is approaches the black line, so $y < Y$ and P_2 comes back ε-close to S_l when P_1 is below it. Therefore, P_1 follows S_l and reach S_r vicinity before P_2, since P_2 pushes the $y-$nullcline of O_1 further to the right. Hence, we have the same situation as during the previous oscillation, yet O_1 and O_2 have exchanged their roles and the sequence repeats, leading to *antiphase synchronization* regime.

(ii) For $c \in (c^d + \delta_4, c^0 - \delta_3)$, the nullclines of O_1 when P_2 comes back ε-close to S_l are represented in Fig. C.19. Thus, when P_2 approaches to the upper fold, P_1 approaches the black line. Consequently, $Y < y$, P_2 remains below P_1, both ε-close to S_l and $X > x$. Hence, P_2 subsequently reaches S_r vicinity before P_1. Therefore, oscillator O_2 keeps on oscillating between S_l and S_r, and prevents P_1 from leaving S_l vicinity. Thus, P_1 oscillates yet remains confined ε-close to S_l and above the projection of the upper fold upon S_l along the x-direction. In this case, the asymptotic periodic behavior is characterized by the *relaxation loss of one oscillator*, see Fig. 4 (a).

(iii) If $c < c^d - \delta_5$, the 6D system admits an attractive equilibrium corresponding to equilibria $(x_{eq}, y_{eq}, z_{eq}) \in S_l$ of O_1 with $X = X_{eq}$ and $(X_{eq}, Y_{eq}, Z_{eq}) \in S_r$ of O_2 with $x = x_{eq}$ (see Fig. C.18). Note that the symmetry in the system implies the existence of another stable equilibrium obtained by exchanging the coordinates between O_1 and O_2. Depending on the initial condition of the 6D system, the associated orbit reaches either one or the other, both cases corresponding to symmetric *total oscillation death*.

In cases 2.(i), (ii) and (iii), the oscillator does not generate MMOs (see panels (a), (b) and (c) of Fig. 4), since each oscillator prevents the $y-$nullcline of the other one from passing through the folds of the critical manifold, where the small oscillations would occur.

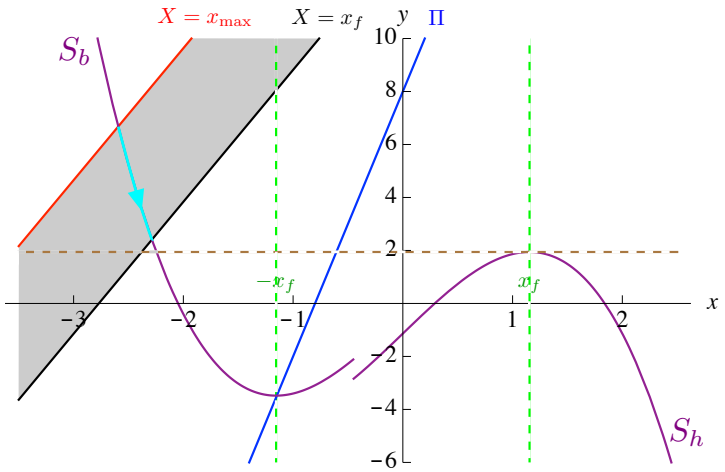

Figure C.19: Projections of the nullclines of oscillator O_1 with parameter values given by 11, $c = -0.502$ and X decreasing from $x_{\max}$ to x_f. We represent in the same plane the two planes $z = z_b$ for $x < x_{on}$ and $z = z_h$ for $x > x_{on}$. In purple, the special curves of the critical manifold S_b and S_h given in eq. (9); in blue, plane Π corresponding to the uncoupled case; the grey area materialize the locus of plane Π_c for X between $x_{\max}$ (red line) and $X = x_f$ (black line). Considering X decreasing between these values, O_1 current point stays close to the stable singular point, which follows the cyan trajectory. The dashed green lines materialize the x-component of the folds $x = -x_f$ and $x = x_f$ and in brown the fast fibers corresponding to the upper fold $\mathcal{F}^+$. In the case of relaxation loss of O_1, its singular point remains above (i.e. has a greater y-component than) the upper fold: the intersection of the black line with the purple curve is above the dashed brown line.

Appendix D. Proof of Theorem 3.2.

First, we consider in system (12) the new time variable

$$s = \tau t. \tag{D.1}$$

We obtain the rescaled system

$$\begin{cases} \dot{x} = -y + f(x) - \phi_f(z), \\ \dot{y} = \varepsilon(x + a_1 y + a_2 + c(x - X)), \\ \dot{z} = \varepsilon \left(\phi_r(x) - \dfrac{z - z_b}{\tau_z} \right), \end{cases} \tag{D.2}$$

$$\begin{cases} \dot{X} = -Y + f(X) - \phi_f(Z), \\ \dot{Y} = \varepsilon(X + a_1 Y + a_2 + c(X - x)), \\ \dot{Z} = \varepsilon \left(\phi_r(X) - \dfrac{Z - z_b}{\tau_z} \right), \end{cases} \tag{D.3}$$

where, now, the dot denotes the derivative w.r.t. the new time variable s. Using the symmetry of the system in the antiphase regime, we will approximate the time that the current point P_1 of O_1 spends along S_r during one cycle. Consider the following set where $\dot{x} < 0$:

$$U_r = \left\{ (x, y, z) \quad \middle| \quad \begin{array}{l} x > x_f, \\ z \in I_z^r \\ y > f(x) - \phi_f(z) \\ y > f(x_{\max}) - \phi_f(z) \end{array} \right\}, \tag{D.4}$$

with I_z^r the $z-$path while $x \in (x_f, x_{\max})$ along $\mathcal{C}(c, \varepsilon)$. When $c \in (c^0 + \delta_2, -\delta_1)$, the oscillators do not possess any equilibrium point on S_r. Since $\dot{x} = 0$ along S_r and $\dot{y} > 0$ in U_r, every orbit starting in U_r escapes from U_r across the half-plane

$$\{(x, y, z) \quad | \quad x = x_f, y > f(x_f) - \phi_f(z)\}. \tag{D.5}$$

From the dynamics of subsystem (D.2), we have also, along any trajectory close to the critical manifold in U_r,

$$\frac{dy}{dx} = \frac{\dot{y}}{\dot{x}} = \frac{\varepsilon(x + a_1 y + a_2 + c(x - X))}{-y + f(x) - \phi_f(z)} < 0 \tag{D.6}$$

and

$$\frac{dy}{dz} = \frac{\dot{y}}{\dot{z}} = \frac{x + a_1 y + a_2 + c(x - X)}{\phi_r(x) - \dfrac{z - z_b}{\tau_z}} > 0. \tag{D.7}$$

It follows from eqs. (D.6)-(D.7) that such a trajectory can be represented as the graph of a differentiable function of (x, z), in particular, the trajectory corresponding to $\mathcal{C}(c, \varepsilon)$. Let us parameterize this trajectory (the intersection of $\mathcal{C}(c, \varepsilon)$ with U_r) as

$$\mathcal{C}_r(c, \varepsilon) : y = \chi^+_{(c,\varepsilon)}(x, z), \quad (x, z) \in (x_f, x_{\max}) \times I^r_z \tag{D.8}$$

and define

$$\psi_r : (x, z, \varepsilon) \to \chi^+_{(c,\varepsilon)}(x, z) - f(x) - \phi_f(z). \tag{D.9}$$

We can directly deduce that $\psi_r > 0$ and is differentiable w.r.t. x and z. Moreover, from classical results [44, 45] on fold-induced slow-fast transitions, there exists ε_0 such that for $\varepsilon \in (0, \varepsilon_0]$, $\mathcal{C}_r(c, \varepsilon)$ remains in a $O(\varepsilon^{2/3})-$neighborhood of $\{(x, f(x) - \phi_f(z), z) | x \in (x_f, x_{\max}), z \in I^r_z\}$. Hence, ψ_r is differentiable in $(x_f, x_{\max}) \times I^r_z \times (0, \varepsilon_0]$, and fulfills statement (30).

By setting $y = f(x) - \phi_f(z) + \psi_r(x, z, \varepsilon)$ into eq. (D.2), we obtain the following 2D reduction of O_1 along the slow manifold

$$\begin{cases} \dot{x} &= \dfrac{\varepsilon}{f'(x) + \frac{\partial \psi_r}{\partial x}(x, z, \varepsilon)} \left[x + a_1(f(x) - \phi_f(z) + \psi_r(x, z, \varepsilon)) + a_2 + c(x - X) \right. \\ & \quad \left. - \left(\phi'_f(z) - \frac{\partial \psi_r}{\partial z}(x, z, \varepsilon) \right) \left(\phi_r(x) - \dfrac{z - z_b}{\tau_z} \right) \right], \\ \dot{z} &= \varepsilon \left(\phi_r(x) - \dfrac{z - z_b}{\tau_z} \right). \end{cases} \tag{D.10}$$

From Proposition 1, statement 2.(b), when $x \in (x_f, x_{\max})$, it forces P_2 to follow a stable quasi-equilibrium point $X_{eq}(x, c)$ on the left sheet of the critical manifold. Thus, we approximate $X \simeq \tilde{X}$ given in eq. (28). Then, the time that variable x spends along the right sheet of the slow manifold during one cycle is given by:

$$T_1(c, \varepsilon) = \frac{1}{\tau} \int_{\mathcal{C}_r(c,\varepsilon)} ds = \frac{1}{\tau} \int_{x_{\max}}^{x_f} \frac{dx}{\dot{x}}, \tag{D.11}$$

where we have already taken into account the rescaling (D.1). From relation (D.11) and system (D.10), direct computations lead to expression (27).

Appendix E. Proof of Theorem 3.3.

Considering the rescaled system (D.2)-(D.3), we approximate the time during which both current points P_1 and P_2 are close to the associated left slow manifold during one cycle.

As previously, due to the symmetry between the oscillators, we consider, without loss of generality, the recovery phase with $x > X$, i.e. O_1 (variables (x, y, z)) is ahead of O_2 (variables (X, Y, Z)). The following proof is based on the same technics as the preceding one. However, we point out a capital difference between the stated results and linked with the boundaries of the integral expressions and quasi-stationary approximations. We recall that the recovery phase that we consider starts just after the fast motion of P_2. Since we can neglect the $O(\varepsilon)$ duration of P_2 fast motion, we can approximate O_1 starting point of the recovery phase by its stable equilibrium, lying on S_l, when $X = x_f$ (corresponding to the end of O_2 active phase). The corresponding x value is then the unique solution $x_0(c) \in (x_{\min}, -x_f)$ of eq. (32).

Similarly as in the proof of Theorem 3.2, we consider the following set where $\dot{x} > 0$:

$$U_l = \left\{ (x, y, z) \;\middle|\; \begin{array}{l} x < -x_f, \\ z \in I_z^l, \\ y < f(x) - \phi_f(z), \\ y < f(x_{\min}) - \phi_f(z) \end{array} \right\}, \tag{E.1}$$

where I_z^l denotes the $z-$path while $x \in (x_{\min}, -x_f)$ along $\mathcal{C}(c, \varepsilon)$. From the same argument as in the previous proof, every orbit starting in U_l escapes from U_l across the half-plane

$$\{(x, y, z) : x = -x_f, y < f(-x_f) - \phi_f(z)\}, \tag{E.2}$$

relations (D.6) and (D.7) are fulfilled, and such a trajectory can be represented as the graph of a differentiable function of (x, z). We denote the intersection of $\mathcal{C}(c, \varepsilon)$ with U_l by

$$\mathcal{C}_l(c, \varepsilon) : y = \chi^-_{(c,\varepsilon)}(x, z), \quad (x, z) \in (x_{\min}, -x_f) \times I_z \tag{E.3}$$

and we pose

$$\psi_l : (x, z, \varepsilon) \to \chi^-_{(c,\varepsilon)}(x, z) - f(x) - \phi_f(z). \tag{E.4}$$

We can directly deduce that $\psi_l < 0$ and is differentiable with respect to x and z. As previously, there exists ε_0 such that for $\varepsilon \in (0, \varepsilon_0]$, $\mathcal{C}_l(c, \varepsilon)$ remains in an $O(\varepsilon^{2/3})-$neighborhood of $\left\{(x, f(x) - \phi_f(z), z) : x \in (x_{\min}, -x_f), z \in I_z^l\right\}$.
1155 Function ψ_l is differentiable in $(x_{\min}, -x_f) \times I_z \times (0, \varepsilon_0]$, and verifies relation (33).

By setting $y = f(x) - \phi_f(z) + \psi_l(x, z, \varepsilon)$ into system (D.2), we obtain the reduced 2D system,

$$\left\{\begin{array}{rcl} \dot{x} & = & \dfrac{\varepsilon}{f(x) + \frac{\partial \psi_l}{\partial x}(x, z, \varepsilon)} \left[x + a_1 \left(f(x) - \phi_f(z) + \psi_l(x, z, \varepsilon)\right) + a_2 + c(x - X)\right. \\ & & \left. - \left(\phi_f'(z) + \frac{\partial \psi_l}{\partial z}(x, z, \varepsilon)\right) \left(\psi_l(x) - \dfrac{z - z_b}{\tau_z}\right)\right], \\ \dot{z} & = & \varepsilon \left(\psi_l(x) - \dfrac{z - z_b}{\tau_z}\right). \end{array}\right. \tag{E.5}$$

During the recovery phase, the current point P_2 of oscillator O_2 follows the left slow manifold and, for any $x \in [x_0(c), -x_f]$, $\dot{X} > 0$. Hence, we can parameterize the X component of trajectory $\mathcal{C}_l(c, \varepsilon)$ by variable x. We keep the dependency w.r.t. c and ε explicit and note this parameterization $\hat{X}(x, c, \varepsilon)$. Then, at the beginning of the recovery phase (after neglecting the $O(\varepsilon)$ duration corresponding to the fast transition from $X = x_f$ to $X = X_{\min}$), x is ε-close to $x_0(c)$. It increases and remains greater than X during the recovery phase which ends when x reaches $-x_f$. Hence, from (E.5), the time spent by P_1 along the left slow manifold from $x = x_0(c)$ to $x = -x_f$ is given by

$$T_2(c, \varepsilon) = \frac{1}{\tau} \int_{\mathcal{C}_l(c,\varepsilon)} ds = \frac{1}{\tau} \int_{x_0(c)}^{-x_f} \frac{dx}{\dot{x}}, \tag{E.6}$$

where we have already taken into account rescaling (D.1). From relation (E.6)
1160 and system (E.5), direct computations lead to expression (31).

Appendix F. Proof of Theorem 3.4.

We need the following technical lemma to prove Theorem 3.4.

Lemma 1. *1 The unique solution $x_0(c)$ of eq. (32) increases with c along $[c^0+\delta_2, -\delta_1]$.*

Proof. By differentiating

$$a_1 f(x_0(c)) + (1+c)x_0(c) + a_2 - cx_f - a_1\phi_f(z_b) = 0$$

w.r.t. c, one obtains

$$a_1 x_0'(c) f'(x_0(c)) + (1+c)x_0'(c) + x_0(c) - x_f = 0$$

and

$$x_0'(c) = \frac{x_0(c) - x_f}{-a_1 f'(x_0(c)) - (1+c)}. \tag{F.1}$$

By construction, for $c \in [c^0+\delta_2, -\delta_1]$, $x_0(c) < -x_f$ ($x_0(c)$ is the x-component of O_1 stable equilibrium lying on S_l): consequently $f'(x_0(c)) < 0$. Recall that $a_1 < 0$ and $c^0+\delta_2 > -1$ as shown in item 2. of Theorem 3.1 leading to $1+c > 0$. Finally $x_0'(c) > 0$.

We now prove Theorem 3.4 and consider a fixed value of $c \in [c^0+\delta_2, -\delta_1]$.

We first prove the decrease of T_1 while c increases. Applying the Leibniz formula to expression (27) defining T_1, we obtain

$$\begin{aligned}\frac{\partial T_1}{\partial c}(c,\varepsilon) &= \frac{1}{\tau}\int_{x_{\max}}^{x_f} \frac{\partial(1/\dot{x})}{\partial c}dx \\ &= \frac{1}{\varepsilon\tau}\int_{x_{\max}}^{x_f} -\frac{(f'(x) + \frac{\partial \psi_r}{\partial x}(x,z,\varepsilon))(x - \tilde{X}(x,c,\varepsilon) - c\frac{\partial \tilde{X}}{\partial c}(x,c,\varepsilon))}{(a_1 f(x) + (1+c)x - c\tilde{X}(x,c,\varepsilon) + k_r(x,z,\varepsilon))^2}dx,\end{aligned} \tag{F.2}$$

where $k_r(x,z,\varepsilon)$ is given in (29). Since $c < 0$, $x > x_f$, $\tilde{X} < 0$, and $\frac{\partial \tilde{X}}{\partial c}(x,c,\varepsilon) > 0$ for O_1 close to its right slow manifold, the integrand in expression (F.2) is positive. The integral being backwards ($x_{\max} > x_f$), the first inequality in the statement follows.

We now prove the decrease of T_2 while c increases. We introduce the following additional notations:

$$\alpha(x,c,\varepsilon) = a_1 f(x) + (1+c)x - c\hat{X}(x,c,\varepsilon) + k_l(x,z,\varepsilon),$$

which is the denominator of the integrand in expression (31) defining T_2. Hence, eq. (31) can be written as

$$T_2(c,\varepsilon) = \frac{1}{\varepsilon\tau}\int_{x_0(c)}^{-x_f} g(x,c,\varepsilon)dx,$$

with

$$g(x,c,\varepsilon) = \frac{f'(x) + \frac{\partial\psi_l}{\partial x}(x,z,\varepsilon)}{\alpha(x,c,\varepsilon)}.$$

Note that function g is directly linked with the x-dynamics of the 2D reduced system (E.5) by

$$\dot{x} = \frac{\varepsilon}{g(x,c,\varepsilon)}.$$

Since $\dot{x} > 0$ for $x < -x_f$ and $X < -x_f$, we have $g(x,c,\varepsilon) > 0$ for $x \in [x_{\min}, -x_f]$ and ε small enough. Moreover, $f'(x) + \frac{\partial\psi_l}{\partial x}(x,z,\varepsilon) < 0$ over $[x_{\min}, -x_f]$, since it is the partial derivative w.r.t. x of the parameterization of $\mathcal{C}_l$ lying exponentially close (w.r.t. ε) to the left slow manifold. Consequently, $\alpha(x,c,\varepsilon) < 0$ above $[x_{\min}, -x_f]$ as well.

Using again the Leibniz formula, we obtain,

$$\frac{\partial T_2}{\partial c}(c,\varepsilon) = \frac{1}{\varepsilon\tau}\left(\int_{x_0(c)}^{-x_f}\frac{\partial g}{\partial c}(x,c,\varepsilon)dx - g(x_0(c),c,\varepsilon)x_0'(c)\right), \tag{F.3}$$

Since

$$\frac{\partial\alpha}{\partial c}(x,c,\varepsilon) = x - \hat{X}(x,c,\varepsilon) - c\frac{\partial\hat{X}}{\partial c}(x,c,\varepsilon),$$

we have

$$\frac{\partial g}{\partial c}(x,c,\varepsilon) = \frac{-(f'(x) + \frac{\partial\psi_l}{\partial x}(x,z,\varepsilon))(x - \hat{X}(x,c,\varepsilon) - c\frac{\partial\hat{X}}{\partial c}(x,c,\varepsilon))}{\alpha^2(x,c,\varepsilon)}.$$

Note that, from $g > 0$ and Lemma 1, $g(x_0(c),c,\varepsilon)\frac{\partial x_0}{\partial c}(c) > 0$. Moreover, $x - X > 0$ along all the recovery phase, $c < 0$ and, as already mentioned, for $x < -x_f$,

$$f'(x) + \frac{\partial\psi_l}{\partial x}(x,z,\varepsilon) < 0.$$

Hence, the sign of the integrand $\frac{\partial g}{\partial c}(x,c,\varepsilon)$ depends on the sign of $x-\hat{X}-c\frac{\partial \hat{X}}{\partial c}$, which is hard to determine: $x-X>0$ during the studied phase, $c<0$ and $\frac{\partial \hat{X}}{\partial c}<0$, but difficult to evaluate. In the following, we prove that the negative term $g(x_0(c),c,\varepsilon)\frac{\partial x_0}{\partial c}(c)$ compensates the integral (i.e. its opposite is greater than the integral) even if $x-\hat{X}-c\frac{\partial \hat{X}}{\partial c}>0$ for some $x\in[x_0(c),-x_f]$. In order to help the track of the signs along the sequence of following equations and inequalities, we write (whenever it is possible) the terms and factors depending on parameters and variables under a positive form with an explicit minus sign ahead if needed.

We first evaluate, using calculation (F.1) in the proof of Lemma 1,

$$g(x_0(c),c,\varepsilon)x_0'(c)=\frac{-f'(x_0(c))-\frac{\partial \psi_l}{\partial x}(x_0(c),z_0,\varepsilon)}{-\alpha(x_0(c),c,\varepsilon)}\frac{x_f-x_0(c)}{a_1f'(x_0(c))+1+c}. \quad \text{(F.4)}$$

We now bound the integral from above, as follows. Consider

$$\frac{\partial \alpha}{\partial x}(x,c,\varepsilon)=a_1f'(x)+1+c+(-c)\frac{\partial \hat{X}}{\partial x}(x,c,\varepsilon)+\frac{\partial k_l}{\partial x}(x,z,\varepsilon).$$

On the one hand, since $x(t)$ and $X(t)$ are strictly increasing along $\mathcal{C}_l(c,\varepsilon)$, we directly obtain, for any $x\in[x_0(c),-x_f]$,

$$\dot{\hat{X}}(t)=\dot{x}(t)\frac{\partial \hat{X}}{\partial x}(x(t),c,\varepsilon)>0 \Longrightarrow \frac{\partial \hat{X}}{\partial x}(x,c,\varepsilon)>0.$$

Moreover, note that $\frac{\partial \hat{X}}{\partial x}$ is $O(1)$ w.r.t. ε. On the other hand, $\frac{\partial k_l}{\partial x}(x,z,\varepsilon)=O(\varepsilon^{2/3})$ and, therefore, its absolute value is bounded from above by $1+c$, for ε small enough. Consequently, $\frac{\partial \alpha}{\partial x}(x,c,\varepsilon)>0$ and we can write

$$\begin{aligned}&\int_{x_0(c)}^{-x_f}\frac{\partial g}{\partial c}(x,c,\varepsilon)dx\\ &=\int_{x_0(c)}^{-x_f}\frac{-(f'(x)+\frac{\partial \psi_l}{\partial x}(x,z,\varepsilon))(\hat{X}(x,c,\varepsilon)-x+c\frac{\partial \hat{X}}{\partial c}(x,c,\varepsilon))}{\frac{\partial \alpha}{\partial x}(x,c,\varepsilon)}\frac{(-\frac{\partial \alpha}{\partial x}(x,c,\varepsilon))}{\alpha^2(x,c,\varepsilon)}dx.\end{aligned} \quad \text{(F.5)}$$

Then, for ε small enough, for any $x\in[x_0(c),-x_f]$,

$$(-c)\frac{\partial \hat{X}}{\partial x}(x,c,\varepsilon)+\frac{\partial k_l}{\partial x}(x,z,\varepsilon)>0,$$

which allows us to obtain

$$\frac{-(f'(x)+\frac{\partial\psi_l}{\partial x}(x,z,\varepsilon))}{\frac{\partial\alpha}{\partial x}(x,c,\varepsilon)} = \frac{-(f'(x)+\frac{\partial\psi_l}{\partial x}(x,z,\varepsilon))}{a_1 f'(x)+1+c+(-c)\frac{\partial\hat{X}}{\partial x}(x,c,\varepsilon)+\frac{\partial k_l}{\partial x}(x,z,\varepsilon)}$$
$$\leq \frac{-(f'(x)+\frac{\partial\psi_l}{\partial x}(x,z,\varepsilon))}{a_1 f'(x)+1+c} = \beta(x). \quad \text{(F.6)}$$

Remark that $\beta(x) > 0$ and that the above notation allows us to write the term evaluated in equation (F.4) as

$$g(x_0(c),c,\varepsilon)\frac{\partial x_0}{\partial c}(c) = \beta(x_0(c))\frac{x_f - x_0(c)}{-\alpha(x_0(c),c;\varepsilon)}. \quad \text{(F.7)}$$

Since $f''(x)$ is positive for $x < 0$ and both $\frac{\partial\psi_l}{\partial x}$ and $\frac{\partial^2\psi_l}{\partial x^2}$ are $O(\varepsilon^{2/3})$, for ε small enough,

$$\beta'(x) = \frac{-f''(x)\left(1+c+(-a_1)\frac{\partial\psi_l}{\partial x}(x,z,\varepsilon)\right)-(1+c)\frac{\partial^2\psi_l}{\partial x^2}(x,z,\varepsilon)}{(a_1 f'(x)+1+c)^2} < 0,$$

and, for any $x \in [x_0(c), -x_f]$,

$$\frac{-f'(x)-\frac{\partial\psi_l}{\partial x}(x,z,\varepsilon)}{\frac{\partial\alpha}{\partial x}(x,c,\varepsilon)} < \beta(x_0(c)).$$

Using this upper bound in (F.5) together with $\max(0, x-\hat{X}-c\frac{\partial\hat{X}}{\partial c}) < \max(x-\hat{X})$, we obtain

$$\int_{x_0(c)}^{-x_f}\frac{\partial g}{\partial c}(x,c,\varepsilon)dx \leq \beta(x_0(c))\max(x-\hat{X})\int_{x_0(c)}^{-x_f}\frac{-\frac{\partial\alpha}{\partial x}(x,c,\varepsilon)}{(\alpha(x,c,\varepsilon))^2}dx$$
$$\leq \beta(x_0(c))\max(x-\hat{X})\left[\frac{1}{\alpha(-x_f,c,\varepsilon)}-\frac{1}{\alpha(x_0(c),c,\varepsilon)}\right]. \quad \text{(F.8)}$$

Since $x_{\min} \simeq -2x_f$ for ε small enough and $x_0(c) < -x_f$,

$$\max(x-\hat{X}) < -x_f - x_{\min} < x_f - x_0(c).$$

Finally, using this inequality, $\beta(x) > 0$, as well as inequality (F.8) and equation (F.7), the derivative of the recovery time w.r.t. c given by (F.3) is bounded from above as follows:

$$\frac{\partial T_2}{\partial c}(c,\varepsilon) \leq \beta(x_0(c))\left[\frac{\max(x-\hat{X})-(x_f-x_0(c))}{(-\alpha(x_0(c),c,\varepsilon))}-\frac{\max(x-\hat{X})}{(-\alpha(-x_f,c,\varepsilon))}\right]$$
$$\leq -\beta(x_0(c))\frac{\max(x-\hat{X})}{(-\alpha(-x_f,c,\varepsilon))} < 0.$$

Hence, both T_1 and T_2 decrease while c increases in $[c^0 + \delta_2, -\delta_1]$, and the approximation $2(T_1 + T_2)$ of the global period decreases, concluding the proof.